CALCULATION OF THE RADIAL ELECTRIC FIELD IN THE DIII-D TOKAMAK EDGE PLASMA

A Dissertation
Presented to
The Academic Faculty

by

Theresa M. Wilks

In Partial Fulfillment
of the Requirements for the Degree
Doctor of Philosophy
Nuclear and Radiological Engineering Program
School of Mechanical Engineering

Georgia Institute of Technology
May 2016

CALCULATION OF THE RADIAL ELECTRIC FIELD IN THE DIII-D TOKAMAK EDGE PLASMA

Approved by:

Dr. Weston Stacey, Advisor
School of Nuclear and Radiological Engineering
Georgia Institute of Technology

Dr. Bojan Petrovic
School of Nuclear and Radiological Engineering
Georgia Institute of Technology

Dr. Robert McGrath
GTRI
Georgia Institute of Technology

Dr. Tris Utschig
School of Nuclear and Radiological Engineering
Georgia Institute of Technology

Dr. Todd Evans
Senior Technical Advisor
General Atomics

Date Approved: March 17, 2016

To all of those in future generations

that will experience harmony

between man and planet

through the power of fusion

ACKNOWLEDGEMENTS

Thank you, family and friends, for your support and love - especially my solid rock, Martin. Thank you Tim Collart and Max Hill, my fellow students in the Fusion Research Center, for your constructive discussions; and Dr. Todd Evans, my co-adviser at General Atomics, for your aid in connecting my theory to experiment. Lastly, Dr. Stacey, my adviser - without your guidance and support this project could not have come to fruition, and your mentorship pushed me to grow both professionally and academically. For all of this I am grateful.

TABLE OF CONTENTS

LIST OF TABLES

LIST OF FIGURES

Page

LIST OF SYMBOLS AND ABBREVIATIONS

φ	Toroidal direction
θ	Poloidal direction
R	Major radius
a	Minor radius
B	Magnetic field
ψ	Enclosed poloidal flux (radial coordinate)
e	Electric charge
δ	Triangularity
κ	Elongation
I_p	Plasma current
p	Pressure
j_r	Radial current density
ϕ	Electrostatic potential
ρ	Normalized radius
f(V)	Velocity distribution function
j	Subscript for main ion, deuterium
k	Subscript for impurity ion, carbon
m	Ion mass
n	Density
E_r^{Ohm}	Predictive radial electric field
E_r^{Exp}	Experimental radial electric field
$\hat{\Gamma}_r$	Radial particle flux

$\Delta V_{\phi,\theta}^{IOL}$	Intrinsic rotation from ion orbit loss
$V_{\phi,\theta}^{fluid}$	Fluid toroidal/poloidal velocity
$V_{\phi,\theta}^{exp}$	Experimental toroidal/poloidal velocity
F_{therm}^{IOL}	Thermal ion orbit loss fraction
f_{fast}^{IOL}	Fast ion orbit loss fraction
R_{loss}^{iol}	Ion non-return fraction
L_{pj}	Pressure gradient scale length
ν_d	Viscous drag frequency
ν_{jk}	Collision frequency
ξ_0	Pitch angle
$\eta_\perp$	Perpendicular resistivity
IOL	Ion orbit loss
SOL	Scrape off layer
NBI	Neutral Beam Injection
RMP	Resonant Magnetic Perturbation
USN	Upper Single Null
LSN	Lower Single Null
FSA	Flux Surface Average
OBM	Outboard Midplane

SUMMARY

The application of a theoretical framework for calculating the radial electric field in the DIII-D tokamak edge plasma is discussed. Changes in the radial electric field are correlated with changes in many important edge plasma phenomena, including rotation, the L-H transition, and ELM suppression. A self-consistent model for the radial electric field may therefore suggest a means of controlling other important parameters in the edge plasma. Implementing a methodology for calculating the radial electric field can be difficult due to its complex interrelationships with ion losses, rotation, radial ion fluxes, and momentum transport. The radial electric field enters the calculations for ion orbit loss. This ion orbit loss, in turn, affects the radial ion flux both directly and indirectly through return currents, which have been shown theoretically to torque the edge plasma causing rotation. The edge rotation generates a motional radial electric field, which can influence both the edge pedestal structure and additional ion orbit losses.

In conjunction with validating the analytical modified Ohm's Law model for calculating the radial electric field, modeling efforts presented in this dissertation focus on improving calculations of ion orbit losses and x-loss into the divertor region, as well as the formulation of models for fast beam ion orbit losses and the fraction of lost particles that return to the confined plasma. After rigorous implementation of the ion orbit loss model and related mechanisms into fluid equations, efforts are shifted to calculate effects from rotation on the radial electric field calculation and compared to DIII-D experimental measurements and computationally simulated plasmas. This calculation of the radial electric field will provide a basis for future modeling of a fast, predictive calculation to characterize future tokamaks like ITER.

CHAPTER 1

INTRODUCTION

1.1 The Motivation for Fusion

In an electrified age using more power than ever, the global population projected to increase to over 9.5 billion people by 2050 [1], and an effort to increase the standard of living of the majority of the existing global population, there is an enormous demand for a clean, efficient, and abundant source of power. The recent Paris Agreement [2] was established to align international efforts to fight emissions that cause climate change, prompting governments around the world to invest in clean energy alternatives such as solar, wind, wave, geothermal, and nuclear technologies. While many of these options will be required to reach reduced emission goals, it is widely accepted that nuclear power is one of the only technologies available that can fully replace the baseload power generation dependence on green-house-gas emitting coal, natural gas, and oil institutions. Conventional nuclear fission is prevalent and relies on the use of mined uranium ore, which is generally abundant on earth. However, there remains an enduring debate regarding the treatment of long lasting radionuclides which are produced from fission reactions. Fusion is an alternative nuclear energy source, which produces roughly four times the amount of energy of a fission reaction with no associated spent fuel comprised of the radiotoxic transuranics in question. The fuel for nuclear fusion is readily found in sea water, providing a long term solution to the clean energy issues the world faces today.

Nuclear fusion for the purpose of power generation is accomplished by making a plasma out of hydrogen isotopes, and heating the reactor core to kilo-electron-volt temperatures in order to reach ignition conditions. However, there is currently no material on earth that is capable of contacting such a hot substance, so the plasma is confined inside of the reactor, or tokamak in this case, through spiraling magnetic fields. Once the

plasma is confined, energy can be injected to heat the plasma to fusion temperatures, and the majority of heat is removed via neutrons produced in from the fusion reaction.

Inside a tokamak, the plasma physics involved in creating the fusion reaction can be complex both to describe mathematically as well as to measure experimentally. The research in this dissertation focuses on understanding the physics that describes a tokamak plasma through modeling, simulation, and comparison with experimental data that was made available by the research team at the DIII-D tokamak, with the goal of contributing to the success of the primary international fusion effort, ITER.

1.2 The Edge Pedestal

There are many indications that tokamak fusion plasma performance in the reactor core will be determined largely by the physics in the far edge region [3-8]. In High confinement mode (H-mode) plasmas, this region is called the "edge pedestal" due to the steep gradients in the radial density, temperature, current, and pressure profiles which influence the main plasma energy confinement and stability. These steep gradients observed in the H-mode edge result in higher plasma densities and temperatures in both the edge and plasma core, leading to overall improved plasma performance. Often referred to as a "transport barrier", this steep gradient region is characterized by strong electromagnetic forces and kinetic particle losses. Usual fluid theory is not sufficient to represent the effect of these phenomena on particle transport, but must be extended to treat non-diffusive electromagnetic "pinch" forces [9] and ion orbit loss [10] of particles on orbits which cross the separatrix. There is also evidence of a strong reduction in turbulent transport suppressed by ExB shear [11-12] in this edge transport barrier. The plasma edge under consideration for this research encompasses roughly the last ten

percent of the plasma poloidal magnetic flux, which translates spatially to a few centimeters just inside the separatrix, or last closed flux surface as seen in Fig. (1).

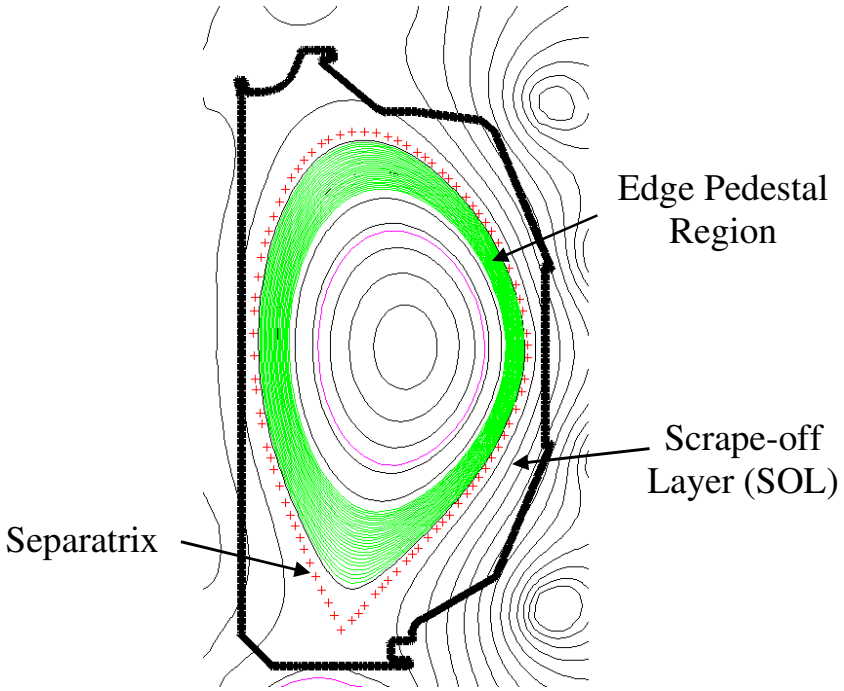

Figure 1: Edge pedestal region of the DIII-D tokamak for an H-mode discharge. (Shaded region represents contours of constant enclosed poloidal magnetic flux between normalized radii 0.85<ρ<1.0).

Not only does the edge pedestal region set limits for core plasma operation like density and temperature, it also defines conditions at the separatrix, which acts as a boundary condition for the open field line region called the scrape off layer (SOL) just inside of the vessel wall. Physics in the SOL is important to understand because it dictates particle and heat removal requirements.

1.3 Radial Electric Field

The transition from the Low-mode (L-mode) to the improved H-mode confinement regime is often associated with an increased radial electric field, E_r, in the edge pedestal region [13-15]. While this transition has been extensively studied and understood relatively well qualitatively, there is still a need for predictive models that can

characterize E_r in current plasmas as well as in future devices. Along with the L-H transition, changes in the edge radial electric field are also correlated with changes in many edge phenomena such as rotation, transport, and the suppression of large magnetohydrodynamic (MHD) instabilities called ELMs (Edge Localized Modes) [16-20]. While the critical gradients and values for these events to occur are set by other mechanisms, such as the peeling-ballooning MHD instability threshold and particle and energy sources and sinks for transport properties, all processes must be constrained by conservation equations.

The equations determining the radial electric field are defined differently inside and outside of the separatrix due to differences in magnetic fields, neutral recycling, and turbulent transport - often leading to a discontinuity at the separatrix. Outside of the separatrix, the radial electric field can be calculated using a parallel Ohm's Law, with charge conservation and assumed boundary conditions on the divertor plates [21]. It is the purpose of this project to define the physics determining the radial electric field inside the separatrix, with a few mechanisms, such as ion orbit loss and return currents, linking the edge plasma to the SOL plasma.

The radial electric field is observable in the edge plasma in most circumstances - smaller in L-mode and ohmic discharges (usually positive), and larger (often negative) in H-mode and Resonant Magnetic Perturbation (RMP) ELM-suppressed discharges. The H-mode can even be triggered by externally inducing a radial electric field in the plasma [22]. This transition is thought to occur because the radial electric field shear suppresses turbulence, and in conjunction with a non-diffusive electromagnetic pinch [23], allows the pedestal to build up to typical H-mode values. When the radial electric field is large

in value and has a “well” shape in the far edge region, intrinsic rotation appears in conjunction with other external torque, which is stabilizing for MHD mode instabilities [24]. Therefore, the structure and presence of the radial electric field has not only been shown to be important, but also suggested as a means of controlling other important edge parameters. To this end, it is desirable to develop a predictive physical model for the radial electric field and its influence on the rest of the plasma that includes mechanisms like ion orbit loss and intrinsic rotation. However, this project first strives to define a self-consistent physical model for the radial electric field calculation before transitioning towards a predictive model that can be used for future reactors like ITER.

Since the radial electric field was identified as a parameter of interest, many transport mechanisms have been explored, such as non-ambipolar diffusive transport [25], curvature and magnetic field gradient drifts [26], increases in the temperature gradient [27], and ion orbit loss [28]. The ion orbit loss mechanism, first introduced by Miyamoto [29], and later extended by Stacey [10] for a computationally attractive formulation for inclusion in predictive or interpretive fluid codes such as GTEDGE [30-32] (discussed later in this work), has been identified as a leading cause for large non-diffusive particle losses in the edge region. There has been significant previous research on ion orbit loss [21,29,33-35], corresponding return currents [35], and their impact on intrinsic rotation [36-39]. Mach probe measurements of velocity peaking in DIII-D have spurred modeling by deGrassie [37] and Stacey [36] to characterize intrinsic rotation from thermal ion losses in the far edge region. Recent XGC0 simulations [40-41] have also supported the theory that ion orbit losses causing highly non-Maxwellian distribution

functions greatly impact the radial electric field, which is closely linked to both diffusive and electromagnetic edge transport processes.

There have been some computational efforts to model the edge plasma in more detail. Hamiltonian guiding center simulations show that a local radial electric field can be generated inside the separatrix due to ion orbit loss [42], and some Monte Carlo orbit following codes, such as the XGC suite and ASCOT can give predictions in agreement with experimental observation [43-45]. Full 2D fluid simulations for the SOL, such as UEDGE and SOLPS5.0, have been developed which can also yield reasonable agreement with experiment [46-48]. However, many simulations do not account for ion orbit loss, and if they do, the radial electric field does not enter the calculation. The most progressive code is the XGC suite, and includes ion orbit loss, the radial electric field, and even turbulence models. While exact models like this are required for future tokamaks like ITER, they can take weeks, or even months to run, suggesting that simpler models are needed for practical, predictive calculations that allow a starting point for the full calculations that the XGC suite can accommodate. Furthermore, most simulations do not account for non-Maxwellian velocity distributions which has been shown experimentally to be important [49]. Both the model presented in this dissertation and the XGC suite strive to account for this distribution change due to ion orbit lost particles, and will be compared in this research.

The present research develops a theoretical framework for how the radial electric field interacts with other edge phenomena such as ion orbit loss, radial particle flux, and rotation velocities, as well as the models necessary to quantify the relationships in the proposed methodology. A modified Ohm's Law is introduced for calculating the radial

electric field in the DIII-D edge pedestal plasma, and validated using the experimental data from three different operational regimes. The Modified Ohm's Law is then extended towards a predictive calculation by employing theoretical neoclassical rotation models which depend on ion orbit loss. To further develop the predictive radial electric field calculation through improvement to rotation calculations, the model extends current ion orbit loss research to account for 1) poloidal dependence of thermal ion orbit loss [50] 2) prompt loss of fast neutral beam ions [51] 3) realistic flux surface geometry and magnetic fields [51] 4) return currents from the SOL [51] 5) incorporation of kinetic ion orbit loss in the fluid continuity and momentum balance equations [51-52] 6) outward streaming lost particles that return to the plasma [51] and 7) x-transport [53]. The improved edge pedestal model and radial electric field calculation is then compared to results from the leadership class XGC0 code housed at PPPL, and the comparative results are used to identify a clear path forward for model improvements in future studies.

CHAPTER 2

BACKGROUND

2.1 Calculational Framework

The edge pedestal is a region of the plasma where many parameters are inter-related. It is often difficult to determine which parameters are the cause for certain observations, and which are effects. While it is beyond the scope of this project to analyze the time dependence of physical occurrences, the complex inter-relationships among parameters are conserved. The general methodology developed for this calculational framework is described by the flow diagram shown in Fig. (2).

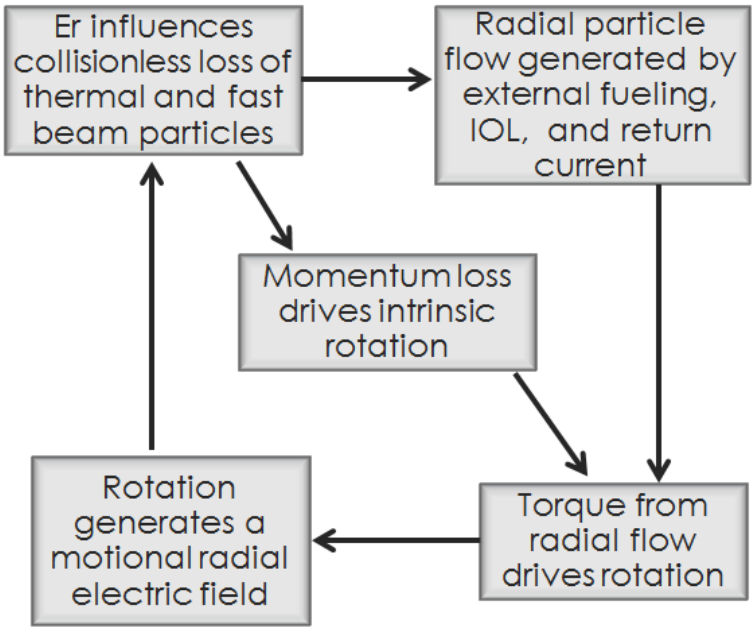

Figure 2: Proposed methodology for calculating the radial electric field, and its qualitative relationship to key other edge parameters such as ion orbit loss, intrinsic rotation, radial particle flux, and rotation velocities.

Five calculations are involved in the methodology of Fig. (2): 1) Ion orbit loss (IOL); 2) Radial particle flux; 3) Intrinsic rotation from IOL; 4) Fluid rotation from momentum balance and 5) Radial electric field from momentum balance. The iterative

calculation is initiated by calculating ion orbit loss using an estimated E_r (e.g. the "experimental" radial electric field when analyzing an experiment). The "experimental" radial electric field is calculated by conserving momentum in the radial direction for the carbon impurity, and can be evaluated using parameters that are all directly measured. The fast and thermal ion orbit losses are then calculated and represented in the continuity equation used to calculate the radial particle flux. To maintain charge neutrality, a radial return current is required to replace the ion orbit lost particles, and this inward current also affects the radial particle flux. The net radial flow of particles constitutes a torque to the plasma that drives rotation in both the poloidal and toroidal directions. There is also an intrinsic rotation caused by ion orbit loss of angular momentum. This plasma rotation generates a motional radial electric field that can be calculated from a modified Ohm's Law equation. This Ohm's Law radial electric field then is used to iterate the above calculations.

The usual method of calculating the "experimental" radial electric field is through the carbon radial momentum balance equation. However, this equation does not dictate the physics for why the radial electric field is present, but is a convenient method for obtaining the profile (which is necessary for the ion orbit loss calculation). The proposed methodology for calculating the radial electric field instead relies on the physical drivers for the field, which are plasma rotation and the ion pressure gradients for all species present in the plasma. In turn, predictive models for rotation and pressure gradient must rely on models for other edge physics processes like ion orbit loss and intrinsic rotation. This dissertation will discuss how ion orbit loss has been extended to fit into the proposed

methodology in Fig. (2) and therefore create a self-consistent framework for calculating the radial electric field.

2.2 GTEDGE

The foundation of this work is rooted in neoclassical plasma theory, which defines the transport physics for a quiescent tokamak plasma and neglects fluctuation driven processes like turbulence [54-55]. The primary computation tool utilized for this project is GTEDGE, which is an in-house Georgia Tech edge pedestal code developed by Stacey that employs fluid particle, momentum, and energy balance equations in conjunction with a two-dimensional neutral recycling model with kinetic corrections for both predictive and interpretive analysis of DIII-D plasmas.

GTEDGE [30-32] takes in experimental radial profiles for densities, temperatures, and velocities, and performs calculations to determine the background plasma and boundary conditions for the edge pedestal. A pinch-diffusion edge pedestal model is used to interpret certain transport quantities like diffusion coefficients and heat diffusivities from the measured data [56]. A particle and energy balance is first applied to the core plasma; then a two-dimensional neutral particle calculation using integral neutron transport theory is used to determine the net ion flux across the separatrix into the SOL. After calculating the inward and outward particle fluxes, the ion densities at the separatrix midplane and divertor plate are calculated using a “two-point” divertor model [30]. With these necessary boundary conditions, the transport of neutrals refueling the plasma edge and the ion density profile are simultaneously calculated. Model parameters are then adjusted to predict the experimental plasma core line average density, energy confinement time, and the central and edge pedestal temperatures.

With the core and edge plasma modeled, quantities of interest such as radial particle flux, rotation velocities, and heat conduction can be calculated for both the main and impurity ions, which are used to determine the radial electric field. These calculations are determined from first principles by conserving particles, momentum, and energy, and are the core of this project. Non-diffusive transport mechanisms such as electromagnetic particle pinch, ion orbit loss and x-transport are incorporated into fluid equations to calculate quantities like the radial particle flux and rotation velocities to interpret various theoretical predictions for the radial electric field.

2.3 DIII-D Diagnostic Systems

For comparative analysis between model and experiment, the plasma model is built using averaged data from representative time slices from DIII-D plasma discharges in various operational regimes. Carbon ion impurity fractions, temperature, and toroidal and poloidal velocity data are measured for each time slice using the Charge Exchange Recombination (CER) system [57]. Usually deuterium data is difficult to directly measure in tokamaks due to the small number of charge states, but for one discharge chosen to be analyzed in this research, the main ion toroidal rotation profiles were measured from the newly developed Main Ion Charge Exchange Recombination (MiCER) system [58-59]. Electron density is measured by Thomson scattering [60] and a multi-channel CO_2 interferometer, and electron temperature is calculated by Thomson scattering. Data processing includes spline fitting the CER ion data, employing a hyperbolic tangent fit to the Thomson scattering electron data, and calculations of radial gradient scale lengths and estimated time derivatives for ion profiles, to provide experimental inputs for the GTEDGE background plasma model.

Plausible errors for the CER system are about 2% of the normalized toroidal flux, and around 3-4% of the normalized toroidal flux for the vertical chord of the Thomson system [61].

2.4 Experimental Data

Three DIII-D discharges described in Table 1 were chosen for validation and analysis of the model described for this project in the flow diagram in Fig. (2).

Table 1: Description of selected DIII-D discharges.

Shot #	Mode	a	δ	κ	I_p	B_φ	P_{beam}	Divertor
123302	H-mode	0.6m	0.37	1.8	1.5 MA	-1.98 T	7.6 MW	LSN
123301	RMP	0.6m	0.27	1.8	1.5 MA	-1.98 T	7.6 MW	LSN
149468	L-mode	0.57m	0.3	1.7	1.2 MA	-2.0 T	5.5 MW	USN

The plasma shape is defined by minor radius (a), triangularity (δ), and elongation (κ). All shots have a significant amount of beam power (P_{beam}) and similar toroidal magnetic fields (B_φ) and plasma currents (I_p). Sister shots #12330(1/2) are typical lower single null (LSN) RMP/H-mode discharges that have been used for many theoretical analyses of experiment [9,62-63]. These discharges have similar operating and background plasma properties, with the primary difference being that the RMP shot is ELM suppressed using 3D magnetic fields produced from the I-coils. The upper single null (USN) L-mode shot #149468 was designed specifically for rotation physics analyses [58-59], and therefore has main ion rotation data available, which was the primary reason for its inclusion in this set. All three shots have edge region collisionalities [64], $\nu^* \sim 0.03 - 0.052$.

The radial profiles of measured electron and ion temperatures, as well as electron densities are shown in Figs. (3)-(4) for the three shots.

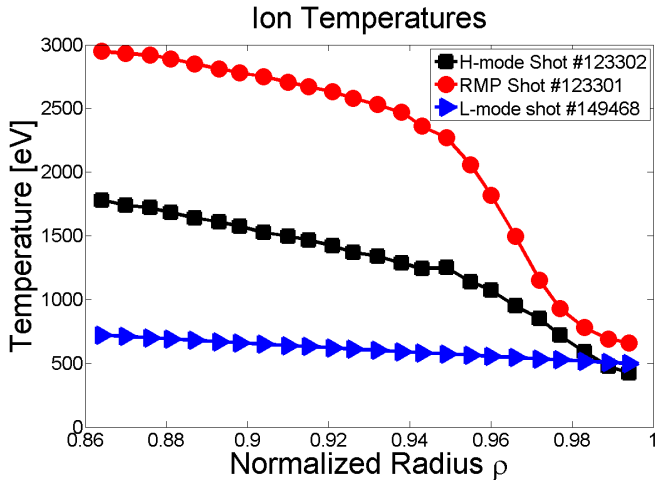

Figure 3: a) Measured ion temperature profiles for H-mode shot #123302, RMP shot #123301, and L-mode shot #149468 b) Measured electron temperature profiles.

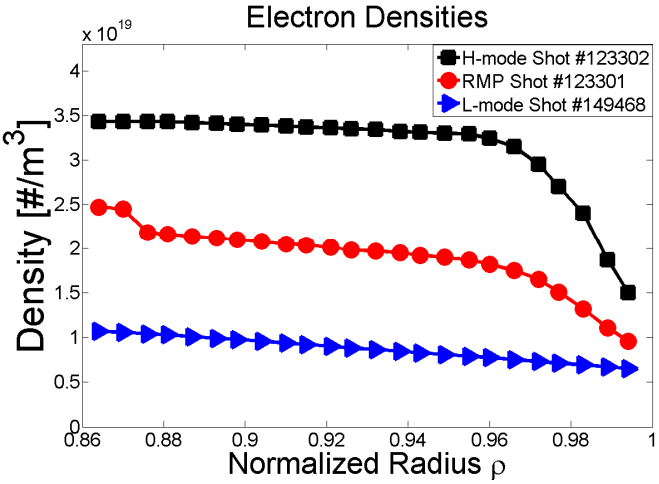

Figure 4: Measured electron density profiles for H-mode shot #123302, RMP shot #123301, and L-mode shot #149468.

Other measured profiles include carbon velocities for shots #12330(1/2) and #149468, and deuterium velocities for #149468, which are shown in Fig. (5).

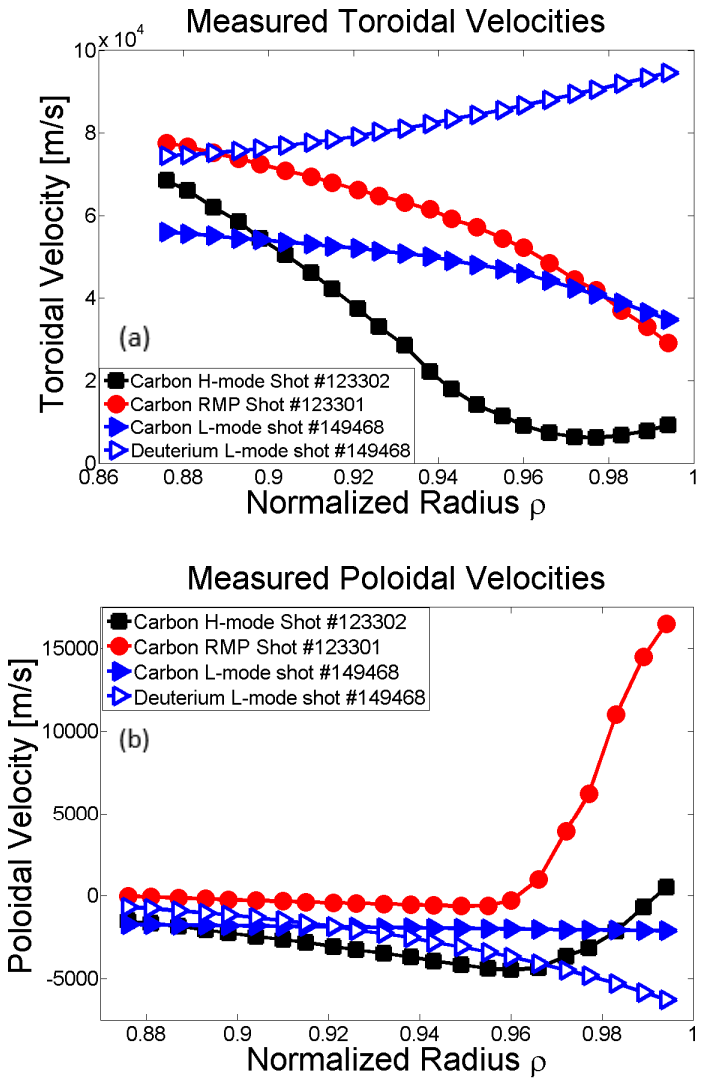

Figure 5: a) Measured toroidal velocity profiles. Carbon profiles are measured for all shots and deuterium is measured for L-mode shot #149468 b) Measured poloidal velocity profiles. Carbon profiles are measured for all shots and deuterium is inferred directly from measurement for L-mode shot #149468.

Measured carbon densities, temperatures, and velocities are used in the radial momentum balance equation for carbon to calculate the "experimental" radial electric

field shown in Fig. (6). This radial electric field profile will be the baseline for the modified Ohm's Law calculation comparison with experiment, whose calculation is discussed in more detail in Chapter 4.

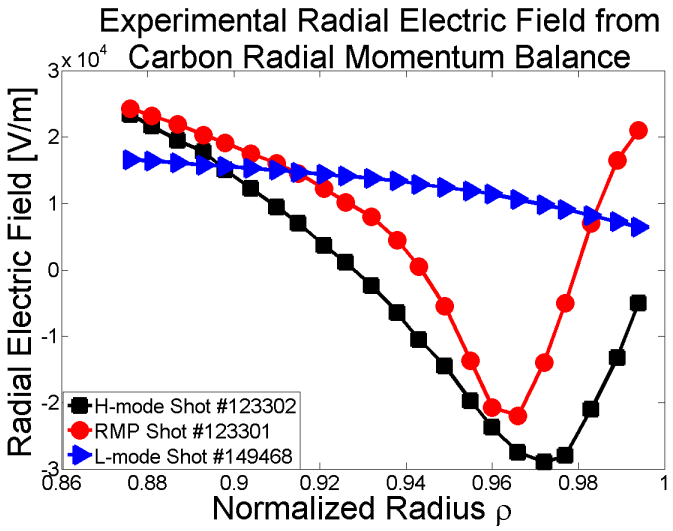

Figure 6: Experimental radial electric fields for all shots calculated from the carbon radial momentum balance equation.

By spanning a broad range of operating parameters, these chosen discharges provide a comprehensive benchmark for validating the modified Ohm's Law calculation of the radial electric field.

CHAPTER 3

ION ORBIT LOSS AND ITS INCLUSION IN PLASMA FLUID THEORY

The first three calculations in Fig. (2) for ion orbit loss, radial particle flux, and intrinsic rotation lay the foundation for the plasma rotation and E_r calculations. The radial particle flux supplies torque to the edge plasma which is important for calculating the rotation velocities (and therefore the radial electric field), and is determined by fueling sources, standard diffusive transport, as well as non-diffusive ion orbit loss phenomena. Therefore to determine the radial electric field, it is first necessary to establish a well-defined ion orbit loss theory, which will be used throughout the calculation described in Fig. (2). Ion orbit loss is a kinetic phenomenon, and its inclusion in fluid theory is nontrivial. The theory for quantifying ion orbit loss in the edge plasma and incorporating its effects into the continuity and momentum balance equations is developed through the models presented in this chapter.

3.1 Standard Ion Orbit Loss Theory

Ion orbit loss theory was first introduced by Miyamoto [29] and later extended by Stacey and Schumman [50] for computational use in GTEDGE. Basic conservation principles are employed to calculate a minimum energy required for ions in the edge plasma with a specific energy, direction, and location to access orbits that cross the separatrix, and are therefore removed from the plasma by collisions with neutrals in the SOL, charge exchange, or being swept into the divertor. This calculation does not track particle orbits, but determines the physical energy requirements for a particle to execute

an orbit with specific initial and final positions. The calculation is based on the conservation of canonical toroidal angular momentum, energy, and magnetic moment.

$$R_s m V_{par,s}\left(\frac{B_{\phi,s}}{B_s}\right) + e\psi_s = \text{constant} = R_0 m V_{par,0}\left(\frac{B_{\phi,0}}{B_0}\right) + e\psi_0 \quad (1)$$

$$\frac{1}{2}m\left(V_{par,s}^2 + V_{perp,s}^2\right) + e\phi_s = constant = \frac{1}{2}m\left(V_{par,0}^2 + V_{perp,0}^2\right) + e\phi_0 \quad (2)$$

$$\frac{mV_{perp,s}^2}{2B_s} = constant = \frac{mV_{perp,0}^2}{2B_0} \quad (3)$$

R is the major radius, m is the mass, V is velocity, B is the magnetic field, ψ is the amount of enclosed poloidal magnetic flux, and φ is the electrostatic potential. The subscripts "perp" and "par" refer to directions perpendicular or parallel to the total magnetic field. The "0" subscripts indicate the values of the quantity on a reference internal flux surface, ψ_0, in the edge region. The second surface required to satisfy these conservation equations is the separatrix, ψ_s, denoted by the subscript "s". Combining these constraints then leads to a quadratic expression that defines the minimum speed, $V_0 = \sqrt{V_{par,0}^2 + V_{perp,0}^2}$, that an ion with a given direction and location on an internal flux surface must have in order to reach the last closed flux surface, ψ_s.

$$V_0^2\left[\left(\left|\frac{B_s}{B_0}\right|\frac{f_{\phi,0}}{f_{\phi,s}}\right)^2 - 1 + (1-\xi_0^2)\left|\frac{B_s}{B_0}\right|\right] + V_0\left[\frac{2e(\psi_0-\psi_s)}{Rmf_{\phi,s}}\left(\left|\frac{B_s}{B_0}\right|\frac{f_{\phi,0}}{f_{\phi,s}}\xi_0\right)\right] + \left[\left(\frac{e(\psi_0-\psi_s)}{Rmf_{\phi,s}}\right)^2 - \frac{2e(\phi_0-\phi_s)}{m}\right] = 0 \quad (4)$$

$f_\varphi = |B_\varphi/B|$ and ξ_0 is the cosine of the particle direction with respect to the toroidal magnetic field on the initial flux surface ψ_0. This minimum velocity is numerically calculated for each flux surface at various poloidal locations, and for several ξ_0 values, and is shown in Fig. (7) as a function of pitch angle.

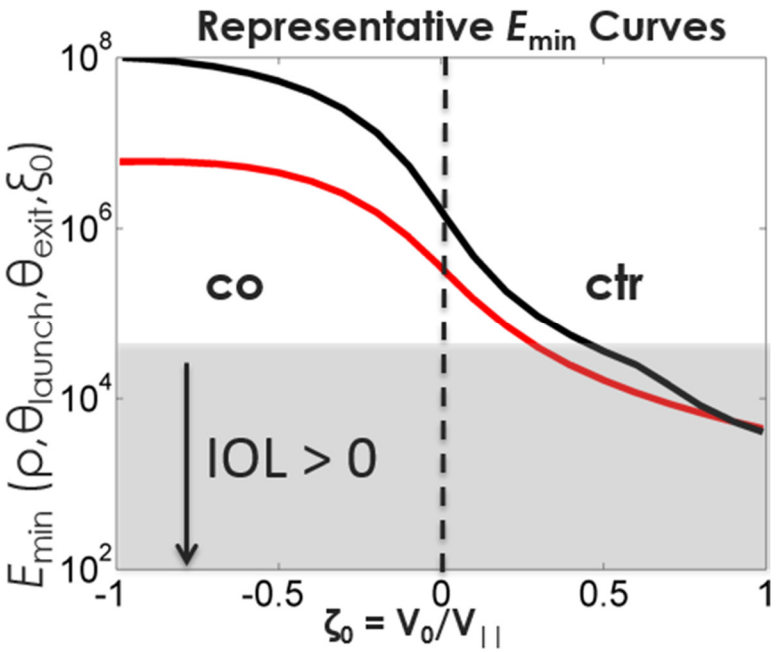

Figure 7: Representative minimum energy curves for a particle to be ion orbit lost as a function of pitch angle.

If Eq. (4) cannot be solved with local plasma parameters, it is assumed that no particles satisfy the requirements to be ion orbit lost in that situation. Even if a minimum escape energy exists physically, there must be particles on the flux surface with enough energy to execute the loss orbits for there to be an effect on the plasma. The shaded region in Fig. (7) illustrates energies that plasma ions may have given a local plasma distribution function whose loss have impact on the plasma edge region (i.e. not many particles in the co-current direction will have energies above 10^8 eV, but many counter current particles will have energies above 10^4 eV in this example).

The minimum energy is seen to decrease for counter-current ions, demonstrating the directional dependence of ion orbit loss, and hence the capability of a momentum source or sink in the fluid equations. Considering this calculation as a function of radius, the minimum energy also monotonically decreases as the launch surface approaches the

separatrix. The distribution of particle velocities on each flux surface can then be compared to the minimum escape velocity, and integrating over the velocity space yields the total fraction of lost particles, which is directly used to calculate the radial particle flux described in the next section.

$$F_{therm}^{IOL} = \frac{N_{loss}}{N_{total}} = \frac{R_{loss}^{iol}\int_{-1}^{1}[\int_{V_{0,min}}^{\infty} V_0^2 f(V_0)dV_0]\,d\xi_0}{2\int_0^{\infty} V_0 f(V_0)dV_0} = \frac{R_{loss}^{iol}\int_{-1}^{1}\Gamma\left(\frac{3}{2},\epsilon_{\min(\xi_0)}\right)d\xi_0}{2\Gamma\left(\frac{3}{2}\right)} \quad (5)$$

R_{loss}^{iol} is the fraction of particles that cross the separatrix on loss orbits and do not return to the plasma, Γ is the gamma function, f(V_0) is the Maxwellian distribution function over velocity space, and $\epsilon_{\min(\zeta_0)} = mV_{0,min}^2(\xi_0)/2kT_{ion}$. A similar cumulative fraction can be calculated for energy loss using the same expression as Eq. (5), but instead taking an energy moment, $\frac{1}{2}mV_0^2$, of the integral. Figure (8) shows representative cumulative particle and energy loss fractions from the H-mode discharge.

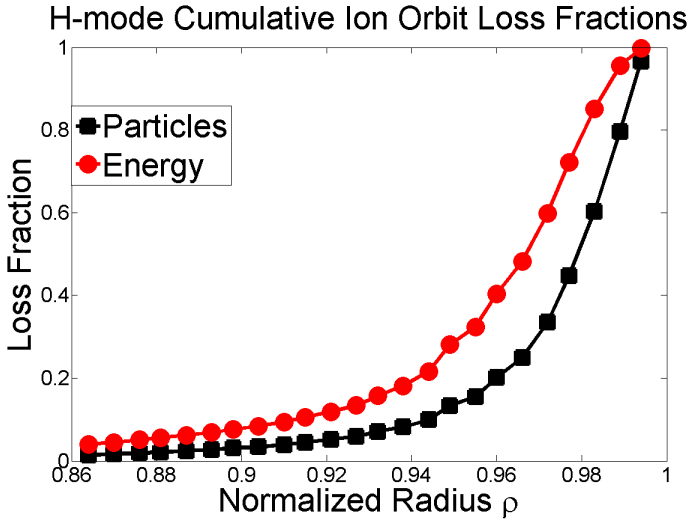

Figure 8: Cumulative particle and energy ion orbit loss fractions.

When computationally employed, this calculation is fully differential in four dimensions [50]: 1) radial variable, ρ 2) initial poloidal location, θ_0 3) final poloidal location on the separatrix, θ_s 4) pitch angle, ξ_0, which allows the distribution function to

evolve due to the changing velocity loss cone structure in the outer flux surface regions close to the separatrix.

A similar process can be followed for the momentum fraction, but with a moment of $mV_0\xi_0$ applied to the velocity integral [10].

$$M_{therm}^{IOL} = \frac{M_{loss}}{M_{total}} = \frac{R_{loss}^{iol}\int_{-1}^{1}[\int_{V_{0,min}}^{\infty}(mV_0\xi_0)V_0^2 f(V_0)dV_0]\,d\xi_0}{2\int_0^{\infty}(mV_0)V_0 f(V_0)dV_0}$$

$$= \frac{R_{loss}^{iol}\int_{-1}^{1}\Gamma\left(2,\epsilon_{\min(\xi_0)}\right)d\xi_0}{2\Gamma(2)} \qquad (6)$$

Because the numerator of this fraction is the net ion orbit momentum loss, an IOL intrinsic rotation for ion species "j" in the toroidal and poloidal directions can be defined for use in calculating the rotation velocity profiles required for the radial electric field calculation [36]

$$\Delta V_{\phi,\theta,j}^{IOL} = \left|\frac{B_{\phi,\theta}}{B_{tot}}\right|\Delta V_{\parallel}^{IOL} = 2\pi\left|\frac{B_{\phi,\theta}}{B_{tot}}\right|\int_{-1}^{1}d\xi_0\left[\int_{V_{0,\min(\xi_0)}}^{\infty}(V_0\xi_0)V_0^2 f(V_0)dV_0\right]$$

$$= \frac{2}{\sqrt{\pi}}\left|\frac{B_{\phi,\theta}}{B_{tot}}\right| M_{therm}^{IOL}\sqrt{\frac{2kT_j}{m_j}} \qquad (7)$$

The intrinsic velocity contribution from the loss of thermalized ions, $\Delta V_{\phi j}^{IOL}$ is usually in the co-current direction due to the preferential loss of counter-current ions [36]. The integral over the cosine of the direction of ions with respect to the magnetic field, ξ_0, accounts for the net momentum loss contribution, and the velocity integral spans the minimum energy required for ion orbit loss [10], $V_{0,min}$, to infinity. A truncated Maxwellian distribution, $f(V_0)$, is assumed to calculate the differential variation in the loss fraction for the distribution function with radius [50]. Net intrinsic rotation for both carbon and deuterium, shown in Fig. (9), exhibits a peaked structure from this

preferential loss of counter current particles. When most or all of the counter current particles are lost, a sufficient minimum energy is reached for co-current ions to be ion orbit lost. The net momentum then starts to decrease due to the reversed directionality of the lost momentum.

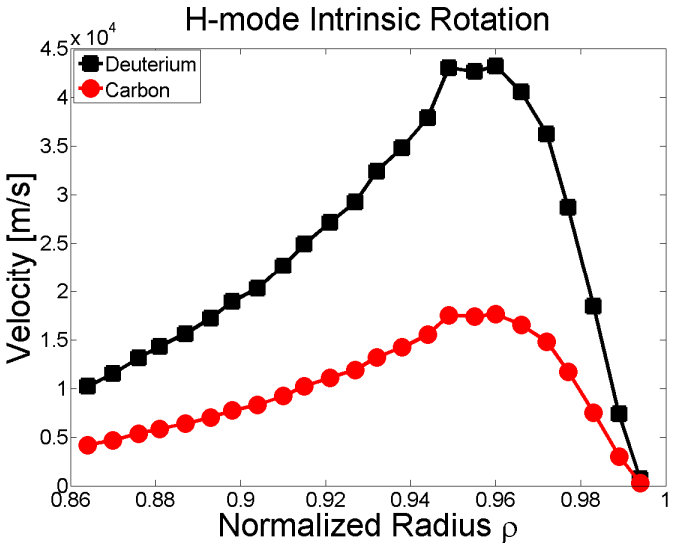

Figure 9: Intrinsic rotation profiles for carbon and deuterium due to ion orbit momentum loss.

Note that this calculation is applicable for any lost ions such as impurities and alpha particles, where the latter are neglected here but will be important in the consideration of future reactors. It is assumed that the return current ions rejoining the plasma from the scrape off layer have negligible momentum, and are not considered in the intrinsic rotation calculation. Theoretically, fast ion losses could also be included in the intrinsic rotation calculation, and MAST experiments have shown that in low aspect ratio machines, there can be more momentum deposited in the plasma than originally injected by neutral beams [35]. In this research, however, a simplified model is used with

a multiplier on the co-current neutral beam injected momentum, which is considered to be 1.0.

3.2 Radial Particle Flux

The radial particle flux , $\hat{\Gamma}_{rj}$, is determined by the continuity equation, which is modified due to fast and thermal ion orbit lost particles instantaneously leaving the plasma.

$$\nabla \cdot \hat{\Gamma} = n\nu_{ion} + S_{nbi}\left(1 - 2f_{fast}^{IOL}\right) - 2\hat{\Gamma}_{\mathrm{rj}} \frac{\partial F_{therm}^{IOL}}{\partial r} \tag{8a}$$

$$\nabla \cdot \hat{\Gamma} = n\nu_{ion} + \hat{S}_{nbi}(r) - 2\hat{\Gamma}_{\mathrm{rj}} \frac{\partial F_{therm}^{IOL}}{\partial r} \tag{8b}$$

The ionization source due to recycling neutrals is calculated using steady state integral neutron transport theory [30]. The majority of the neutral beam source in the core is seen as a boundary condition, but there is also a deposition profile calculated from the neutral beam code NBeams [65] used to define the source as a function of radial coordinate in the edge region used in the model. Both the core and edge NBI sources are reduced by the fast ion orbit loss fraction, $f_{fast}^{IOL}(r)$, which represent mono-energetic (one of three energy components) and mono-pitch-angled particles that are promptly lost upon ionization in the plasma. Thermalized ions can also be lost by executing loss orbits, and these particles are removed through the derivative of the cumulative thermal loss fraction, $\frac{\partial}{\partial r} F_{therm}^{IOL}(r)$, which represents the number of ion orbit lost particles from flux surface "r" inside the separatrix. The thermal ion orbit loss fraction is applied directly to the radial particle flux which is initially comprised of a Maxwellian distribution of particles, and through the edge region loses significant amounts of counter-current particles such that the distribution function at the separatrix is highly non-Maxwellian.

To maintain charge neutrality, there must be an inward compensating return current from the scrape off layer with divergence equal in magnitude to the lost charge from ion orbit loss in the differential interval dr at location r. The combined effects of instantaneous particle losses plus the inward return current results in twice the reduction of the radially outward particle flux due to ion orbit loss alone (and hence the multiplier of 2 in the ion orbit loss terms in the continuity equation). The calculation of the fast ion orbit loss fractions will be discussed in more detail in Chapter 5. Solving Eq. (8) in cylindrical coordinates yields the integral expression for the radial particle flux.

$$\hat{\Gamma}(r) = \int_0^r \frac{r'}{r} S_{tot}(r') e^{-2[F_{therm}^{IOL}(r) - F_{therm}^{IOL}(r')]} dr' \tag{9a}$$

$$S_{tot}(r') = n(r')\nu_{ion}(r') + \hat{S}_{nbi}(r') \tag{9b}$$

The "carat" above the Gamma and NBI source symbols represent that the variable has been corrected for ion orbit loss. A similar equation can be written for the impurity species, which is assumed to be negligible because the plasma is in equilibrium. With no internal carbon source, the outward carbon flux balances the inward carbon flux from the scrape off layer. The radial particle flux both with and without thermal ion orbit loss is shown in Fig. (10). The model for including fast ion orbit losses and its impact on Eq. (9) will be developed and analyzed in Chapter 6.

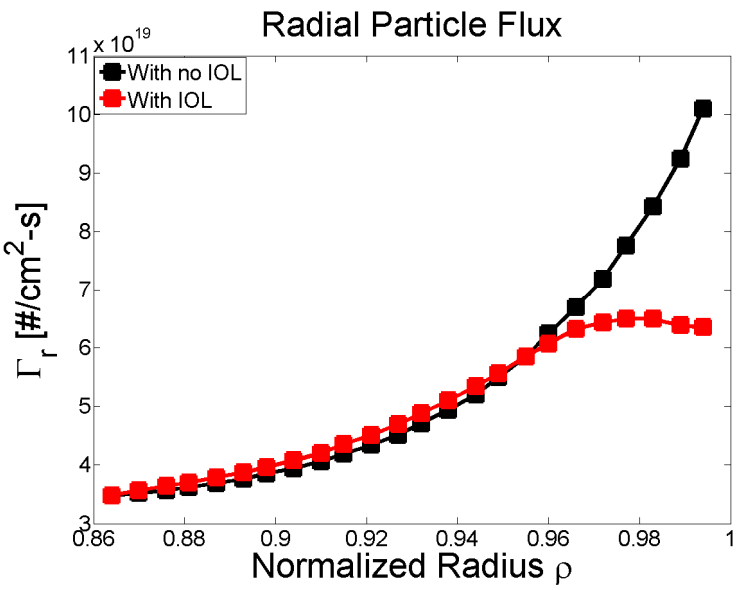

Figure 10: Radial particle flux calculated from the continuity equation with and without ion orbit loss for DIII-D H-mode shot #123302.

The radial particle flux without the correction of IOL monotonically increases towards the separatrix because the density of recycling neutrals, and hence the source of ionization, is constantly increasing towards the wall. This would be an expected profile for electrons, which are assumed not to be kinetically lost because they are sufficiently bound to the magnetic field lines. However, when the radial ion particle flux is corrected for IOL, the flux decreases in the far edge region both because outflowing ions are lost by IOL and because of the negative sign of the inflowing ion flux from the scrape off layer necessary to maintain charge neutrality.

3.3 Relationship between Intrinsic Rotation and Net Momentum

Like the particle balance equation, kinetic effects of ion orbit loss must also be accounted for in the momentum balance equations. However, this task is not as straightforward in the directionally dependent momentum balance equation as in the continuity equation.

The first velocity moment of the Boltzmann equation for a given plasma species "i" describes the vector momentum balance equation.

$$m_i \frac{\partial (n_i \boldsymbol{v_i})}{\partial t} + \nabla \cdot \boldsymbol{M}_i - n_i e_i (\boldsymbol{E} + \boldsymbol{v_i} \times \boldsymbol{B}) = \boldsymbol{F_i^1} + \boldsymbol{S_i^1} \qquad (10)$$

Where **M** is the (inertial plus momentum) stress tensor, **E** is the electric field, $\boldsymbol{v}$ is the ion velocity, **B** the magnetic field, $\mathbf{F^1}$ the collisional friction term, and $\mathbf{S^1}$ the source first velocity moment. Components of Eq. (10) can now be considered in a similar manner to the above treatment of ion orbit loss in the radial particle flux in Eq. (8).

An analogous implementation of ion orbit momentum loss into the toroidal momentum balance equation would require the retention of radial derivatives of the toroidal velocity in the stress tensor and inertial terms, along with radial integration of the resulting toroidal momentum equations. However, the usual treatment [66] of the toroidal viscous torque leads to a form which can be written as the sum of the "parallel", "gyroviscous", and "perpendicular" components, where the "parallel" component identically cancels in the flux surface average in an axi-symmetric tokamak [67]. The remaining components of the neoclassical viscous stress tensor in an axi-symmetric tokamak can be can be written in the form of "drag" terms [68-69], $nm\nu_{visc}V_\phi$ and $nm\nu_{inert}V_\phi$, where ν_{visc} and ν_{inert} are given in reference 69. This model subsumes the radial derivatives of the toroidal velocity into the drag frequency terms. Therefore, a toroidal momentum balance equation with ion orbit loss inherently included would require a new rotation model that retains the radial toroidal velocity derivatives explicitly in the primary balance equation. Since the derivation of a new rotation model is beyond the scope of this work, an ad hoc correction for ion orbit loss through the external momentum source in the toroidal momentum balance equations is introduced. Using

neoclassical viscosity models, the toroidal momentum balance equation is defined for a toroidally axi-symmetric tokamak [69-71].

$$B_\theta e_j \hat{\Gamma}_{rj} + n_j e_j E_\phi = n_j m_j \nu_{dj} V_{\phi j} + n_j m_j \nu_{jk} (V_{\phi j} - V_{\phi k}) - M_{\phi j} \tag{11}$$

This formalism also describes impurities, which is represented by the "k" subscript and summing over multiple species "k" where appropriate, but the present analysis considers a two species plasma comprised of the main ion deuterium, "j", and impurity carbon, "k". For neoclassical theory , $\nu_{visc} = \nu_{gyro}$, the gyroviscous drag [68]. More generally , $\nu_{dj} = \nu_{visc,j} + \nu_{inertia,j} + \nu_{atomic,j} + \nu_{anom,j}$, which multiplies the main ion toroidal angular momentum to represent the toroidal angular momentum exchange rate due to toroidal viscosity, toroidal inertia, atomic physics, and anomalous processes such as turbulence.

The external momentum source, $M_{\phi j}$, in Eq. (11) is comprised of neutral beams in these calculations, but can possibly include other external or effective internal momentum sources such ion orbit momentum loss. The kinetically derived momentum ion orbit loss can be expressed as either an external momentum source or an intrinsic rotation. In cases when an effective momentum source is the preferred method, the external momentum source is expanded to not only include neutral beam injection, but also ion orbit loss.

$$\mathrm{M_{\phi j/k}} = \mathrm{M^{NBI}_{\phi j/k}} + \mathrm{M^{IOL}_{\phi j/k}} \tag{12}$$

The external ion orbit loss momentum term can then be derived by solving the toroidal momentum balance equation, Eq. (11), both with and without $\mathrm{M^{IOL}_{\phi j/k}}$ for the difference in velocity defined by the intrinsic rotation in Eq. (7). The expressions for the net ion orbit loss momentum sources in the toroidal momentum balance equation for both species become

$$\mathrm{M^{IOL}_{\phi j}} = \mathrm{n_j m_j}\left[\left(\nu_{\mathrm{jk}} + \nu_{\mathrm{dj}}\right)\Delta \mathrm{V^{IOL}_{\phi j}} - \nu_{\mathrm{jk}} \Delta \mathrm{V^{IOL}_{\phi k}}\right] \tag{13a}$$

$$M_{\phi k}^{IOL} = n_k m_k \left[\left(\nu_{kj} + \nu_{dk} \right) \Delta V_{\phi k}^{IOL} - \nu_{kj} \Delta V_{\phi j}^{IOL} \right] \quad (13b)$$

Solutions to the fluid toroidal momentum balance equation with the ion orbit loss included as an effective momentum source would be satisfied by the experimentally measured velocities. Alternatively, Eq. (11) can be solved with the external momentum source excluding ion orbit loss effects, $M_{\phi j/k} = M_{\phi j/k}^{NBI}$. This yields solutions through the use of "fluid" velocities, $V_{\phi j}^{fluid} = V_{\phi j}^{exp} - \Delta V_{\phi j}^{IOL}$, which do not take into account the presence of intrinsic rotation, but does take into account the ion orbit particle losses in the radial particle flux, $\hat{\Gamma}_{rj/k}$. To verify this, the total momentum source from Eq. (12) is used in the toroidal momentum balance equations with the experimental velocities, and rearranged so that the velocity terms are aggregated.

$$n_j m_j \left\{ \nu_{jk} \left[\left(V_{\phi j}^{exp} - \Delta V_{\phi j}^{IOL} \right) - \left(V_{\phi k}^{exp} - \Delta V_{\phi k}^{IOL} \right) \right] + \nu_{dj} \left(V_{\phi j}^{exp} - \Delta V_{\phi j}^{IOL} \right) \right\}$$
$$= B_\theta e_j \hat{\Gamma}_{rj} + n_j e_j E_\phi^A + M_{\phi j}^{NBI} \quad (14)$$

A similar equation can be written with the "j" and "k" subscripts interchanged for the carbon toroidal momentum balance equation. The "fluid" velocities can then be substituted for the experiment minus intrinsic rotation terms in parentheses to yield an identical equation to Eq. (11), except with IOL effects accounted for in the velocities as an intrinsic rotation instead of the net momentum source. Therefore it follows that the correct inclusion of the ion orbit loss effects into the momentum balance equations can be accomplished either by 1) using the intrinsic rotation velocities to modify the fluid velocities and only neutral beams included as an external source or 2) using an effective ion orbit loss momentum source to calculate modified fluid velocities.

It is important to note that the treatment of ion orbit loss as an external momentum source relies on plasma properties like momentum drag frequencies to be

known, while the intrinsic rotation correction can be applied directly to measured velocities. For this reason, ion orbit loss will be included as an intrinsic rotation, not an external momentum source, for the theoretical analyses in this work.

Similar methodology can be used to define either an external momentum source or intrinsic rotation correction for the poloidal momentum balance equations. The external momentum source term for the poloidal momentum balance equations takes the form of Eqs. (15) and will be used more explicitly in the fluid rotation models in Chapter 5.

$$M_{\theta j}^{IOL} = n_j m_j \left[\left(\nu_{jk} + \nu_{visc,j} \right) \Delta V_{\theta j}^{IOL} - \nu_{jk} \Delta V_{\theta k}^{IOL} \right] \tag{15a}$$

$$M_{\theta k}^{IOL} = n_k m_k \left[\left(\nu_{kj} + \nu_{visc,k} \right) \Delta V_{\theta k}^{IOL} - \nu_{kj} \Delta V_{\theta j}^{IOL} \right] \tag{15b}$$

While this follows naturally from the above analysis, an external momentum source due to ion orbit loss in the poloidal direction is not usually observed or predicted.

CHAPTER 4

OHM'S LAW AND THE RADIAL ELECTRIC FIELD

The conventional "experimental" radial electric field is constructed by using the measured carbon density, temperature and rotation velocities discussed in Chapter 2 in the carbon radial momentum balance equation.

$$E_{rc}^{exp} = \frac{1}{Z_c e n_c}\frac{\partial p_c}{\partial r} - V_{\theta c}B_{\phi} + V_{\phi c}B_{\theta} \tag{16}$$

However, this equation does not determine the physics for why the radial electric field exists. This chapter develops an analytical expression for the modified Ohm's Law based on fluid theory to determine the radial electric field in the edge plasma. The theory is validated for use with the three previously described DIII-D discharges by evaluating the expression with data either measured or constructed from measured data and conservation laws, and then comparing the predicted value of the radial electric field with the experimental profile calculated from Eq. (16).

4.1 Derivation of Ohm's Law

Revisiting the vector momentum balance equation from Eq. (10), the total velocity can be decomposed.

$$\boldsymbol{v_i} = \boldsymbol{u_i} + \boldsymbol{y_i} \tag{17}$$

$\boldsymbol{v}$ is the kinetic ion velocity, **u** is the average velocity, and **y** is the random thermal motion (i.e. the relative motion of species "i" with respect to the common mass velocity). The momentum stress tensor can then be decomposed into the inertial and pressure tensor terms. Multiplying Eq. (10) by e_i/m_i , summing over all species, and assuming 1) m_e/m_i << 1 for "i" ≠ "e", 2) the Lorentz friction model, $F_{i,j} = -n_i m_i \nu_{i,j}\left(V_i - V_j\right)$, 3) time

independence, 4) negligible inertia and viscosity, 5) charge neutrality, and 6) no external radial source [72], Eq. (10) yields the fluid momentum balance equation

$$\frac{1}{n_e e_e}\nabla p_{\boldsymbol{e}} = \boldsymbol{E} + \boldsymbol{u}\times\boldsymbol{B} + \frac{1}{n_e e_e}\boldsymbol{j}\times\boldsymbol{B} - \eta\boldsymbol{j} \tag{17}$$

and to lowest order the pressure is constant along flux surfaces.

$$\nabla p = \nabla\left(p_e + p_j + p_k\right) = \boldsymbol{j}\times\boldsymbol{B} \tag{18}$$

where species "j" is now defined to be deuterium, species "k" is the carbon impurity, and electrons are represented by the "e" subscript. With these assumptions as well as $e_e = -e_j$, the radial projection of Eq. (17) can be further simplified to be defined in terms of solely the two ion species while still maintaining the physics of the electron population,

$$\begin{aligned} E_r^{Ohm} &= E_r^{\Omega} + E_r^{UxB} + E_r^{\nabla \mathrm{p}} \\ &= \eta_{\perp,Spitzer} j_r - (\boldsymbol{u}\times\boldsymbol{B})_{\boldsymbol{r}} + \frac{1}{e_j\left(n_j + z_k n_k\right)}\nabla_{\mathrm{r}}\left(p_j + p_k\right) \end{aligned} \tag{19}$$

The Spitzer perpendicular resistivity [73] is

$$\eta_{\perp,Spitzer} = 1.03\times 10^{-4} Z_{eff}\ln(\Lambda)\, T_e^{-\frac{3}{2}} \tag{20}$$

The velocities and pressure gradients can be written explicitly to obtain the final version of the modified Ohm's Law radial electric field which will be used in the subsequent sections.

$$E_r^{Ohm} = -\eta_{\perp,Spitzer} \mathrm{j}_{\mathrm{r}} - \frac{V_{\theta,j}B_\phi - V_{\phi,j}B_\theta}{1 + n_k m_k/n_j m_j} - \frac{V_{\theta,k}B_\phi - V_{\phi,k}B_\theta}{1 + n_j m_j/n_k m_k} - \frac{p_j L_{pj}^{-1} + p_k L_{pk}^{-1}}{e_j\left(n_j + z_k n_k\right)} \tag{21}$$

V_ϕ is the toroidal velocity, V_θ the poloidal velocity, and the pressure gradient scale length for each species is defined as $L_p^{-1} = -\frac{1}{p}\frac{\partial p}{\partial r}$. The radial current is required by charge neutrality to compensate for ion orbit lost particles for both thermal and fast ions.

Assuming that the compensating current is comprised of the main ion species, the total inward current j_r can be defined by

$$j_r = j_{r,IOL}^{thermal} + j_{r,IOL}^{nbi} \tag{22}$$

The first term is the compensating current for the ion orbit loss of thermalized plasma ions, and the second term is the compensating current for the fast neutral beam ions that are ion orbit lost. The radial compensating return current must exactly replace the ion orbit lost particles to maintain charge neutrality by conserving $\nabla \cdot \boldsymbol{j} = 0$ as discussed in detail in Chapter 3.

4.2 Estimated Experimental Velocities

The purpose of this chapter is to develop and validate the modified Ohm's Law expression for E_r of Eq. (21) using the best available information about the rotation and pressure profiles to confirm its consistency with the usual carbon "experimental" electric field which can be calculated by using the radial carbon measurements of density, temperature, and velocities in the carbon radial momentum balance in Eq. (16). This is readily accomplished with the L-mode discharge because both the deuterium and carbon velocity profiles are directly measured. However, a method for determining the deuterium rotation profiles as close to experiment as possible is presented in this section for the H-mode and RMP discharges.

4.2.1 Toroidal Velocity

The radial particle flux due to ion orbit loss, $\Gamma_{rj}^{IOL} = {j_r}/{e} = \Gamma_{rj}\left(f_{fast}^{IOL} = 0, F_{therm}^{IOL} = 0\right) - \Gamma_{rj}\left(f_{fast}^{IOL}, F_{therm}^{IOL}\right)$, can be used to calculate the net radial current used in the modified Ohm's Law expression.

$$E_r^{\Omega} = \eta_{\perp,Spitzer} j_r = 1.03 \times \frac{10^{-4} Z_{eff} \ln(\Lambda)}{T_e^{3/2}} e\Gamma_{rj}^{IOL} \tag{23}$$

To determine the motional component, $E_r^{\mathrm{U}\times\mathrm{B}}$, toroidal and poloidal rotation velocities are required for both ion species. With no main ion measurements for the RMP and H-mode discharges, a method for estimating the deuterium rotation profiles is required. It is assumed that the experimental velocity is a superposition of the velocity obtained from the fluid equations and intrinsic rotation from ion orbit loss [52].

$$V_{\phi j}^{exp} = V_{\phi j}^{fluid} + \Delta V_{\phi j}^{IOL} \tag{24}$$

The experimentally measured velocities, $V_{\phi j}^{exp}$, are distinguished from the fluid velocities, $V_{\phi j}^{fluid}$, which satisfy the momentum balance Eq. (11), by the inclusion of intrinsic rotation due to ion orbit loss for each species as discussed in section 3.3.

First order perturbation theory is utilized to determine an "experimental" deuterium toroidal fluid velocity which satisfies the momentum balance equations, as well as drag frequencies, ν_{dj} and ν_{dk}, from the measured carbon velocity profile [61].

$$V_{\phi j}^{fluid} = V_{\phi k}^{fluid} + \Delta V_{\phi}^{pert} \tag{25}$$

Eq. (26) is then used to obtain the total deuterium velocity.

$$V_{\phi j}^{exp} = \left(V_{\phi k}^{exp} - \Delta V_{\phi k}^{IOL} + \Delta V_{\phi j}^{IOL}\right) + \Delta V_{\phi}^{pert} \tag{26}$$

The perturbation theory is developed first by summing the toroidal momentum balance Eq. (11) for both species, and defining a composite toroidal momentum transport frequency,ν_d^0.

$$\nu_d^0 \equiv \frac{n_j m_j \hat{v}_{dj} + n_k m_k \hat{v}_{dk}}{n_j m_j + n_k m_k}$$

$$= \frac{(n_j e_j E_\phi + e_j B_\theta \Gamma_{rj} + M_{\phi j}) + (n_k e_k E_\phi + e_k B_\theta \Gamma_{rk} + M_{\phi k}) - n_j m_j \hat{v}_{dj} \Delta V_\phi^{pert}}{(n_j m_j + n_k m_k)(V_{\phi k} - \Delta V_{\phi k}^{IOL})} \quad (27)$$

Initially setting the small parameter ΔV_ϕ^{pert} in Eq. (27) to zero results in the zeroth order approximation of the composite drag frequency, ν_d^0. This quantity can be used in Eq. (28) to obtain a toroidal perturbative quantity, ΔV_ϕ^{pert}, which depends on the measured carbon toroidal velocity along with other measured parameters.

$$\Delta V_\phi^{pert} = \frac{(n_j e_j E_\phi + e_j B_\theta \Gamma_{rj} + M_{\phi j}) - n_j m_j \hat{v}_{dj}^0 V_{\phi k}}{n_j m_j (\nu_{jk} + \hat{v}_{dj})} \quad (28)$$

Continuing the perturbation analysis, from Eq. (27) it is found that the main ion species drag is

$$\hat{v}_{dj} \cong \nu_d^1$$

$$= \frac{(n_j e_j E_\phi + e_j B_\theta \Gamma_{rj} + M_{\phi j}) + (n_k e_k E_\phi + e_k B_\theta \Gamma_{rk} + M_{\phi k}) - n_j m_j \hat{v}_d^0 \Delta V_\phi^{pert}}{(n_j m_j + n_k m_k)(V_{\phi k} - \Delta V_{\phi k}^{IOL})} \quad (29)$$

and the carbon impurity drag frequency is

$$\hat{v}_{dk} \cong \frac{(n_k e_k E_\phi + e_k B_\theta \Gamma_{rk} + M_{\phi k}) + n_k m_k \hat{v}_{kj} \Delta V_\phi^{pert}}{n_k m_k (V_{\phi k} - \Delta V_{\phi k}^{IOL})} \quad (30)$$

It is important to note that the perturbation theory assumes that the difference in the deuterium and carbon fluid velocities is small. Iteration to find a simultaneous solution for the perturbation value and the drag frequency converges on a solution for which $|\Delta V_\phi / V_{\phi k}| \ll 1$, which is consistent with the use of perturbation techniques for these discharges.

The L-mode discharge can be used as a check of the perturbation theory because both deuterium and carbon toroidal velocities are directly measured. The "fluid" velocity obtained for deuterium by subtracting the intrinsic rotation ($V_{\phi j}^{fluid} = V_{\phi j}^{exp} - \Delta V_{\phi j}^{IOL}$) in Fig. (11) is in good agreement with the perturbation theory calculation ($V_{\phi j}^{fluid} = V_{\phi k}^{fluid} + \Delta V_{\phi}^{pert}$).

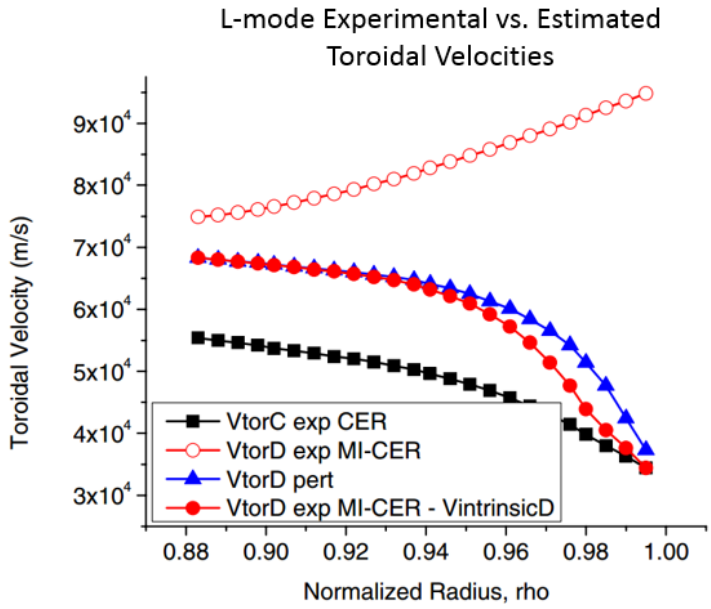

Figure 11: Comparison of perturbation theory to experimental and fluid (no IOL effects of intrinsic rotation) velocities for L-mode shot #149468. (Re-produced from Nucl. Fusion 54, 073021 (2011) with permission.)

4.2.2 Poloidal Velocity

Perturbation theory is not appropriate for estimates of poloidal velocity profiles because calculated deuterium poloidal rotation can be quite different than that of the carbon impurity, and there are no other techniques for inferring poloidal momentum transport frequencies from experiment.

For the purposes of evaluating Eq. (21) with velocities closest to experiment, the radial momentum balance equations for deuterium and carbon are used. The deuterium poloidal velocity is defined by the radial deuterium momentum balance,

$$V_{\theta j} = \frac{1}{B_\phi}\left(B_\theta V_{\phi j} - E_{rc}^{exp} + \frac{1}{n_j e_j}\frac{\partial p_j}{\partial r}\right) \tag{31}$$

using the usual experimental radial electric field defined by the carbon radial momentum balance and evaluated with purely measured parameters from Eq. (16) and shown in Fig. (6).

By combining Eqs. (16) and (31), an expression for the "experimental" deuterium velocity can be constructed from the radial momentum balance for the two species.

$$V_{\theta j} = V_{\theta k} - \frac{1}{B_\phi}\left(\frac{1}{e_j n_j}\frac{\partial p_j}{\partial r} - \frac{1}{e_k n_k}\frac{\partial p_k}{\partial r}\right) + \frac{B_\theta}{B_\phi}\left(V_{\phi j}^{exp} - V_{\phi k}^{meas}\right) \tag{32}$$

Both measured and estimated rotation velocity profiles for carbon and deuterium are summarized in Fig. (12) for the three DIII-D discharges described in Table 1.

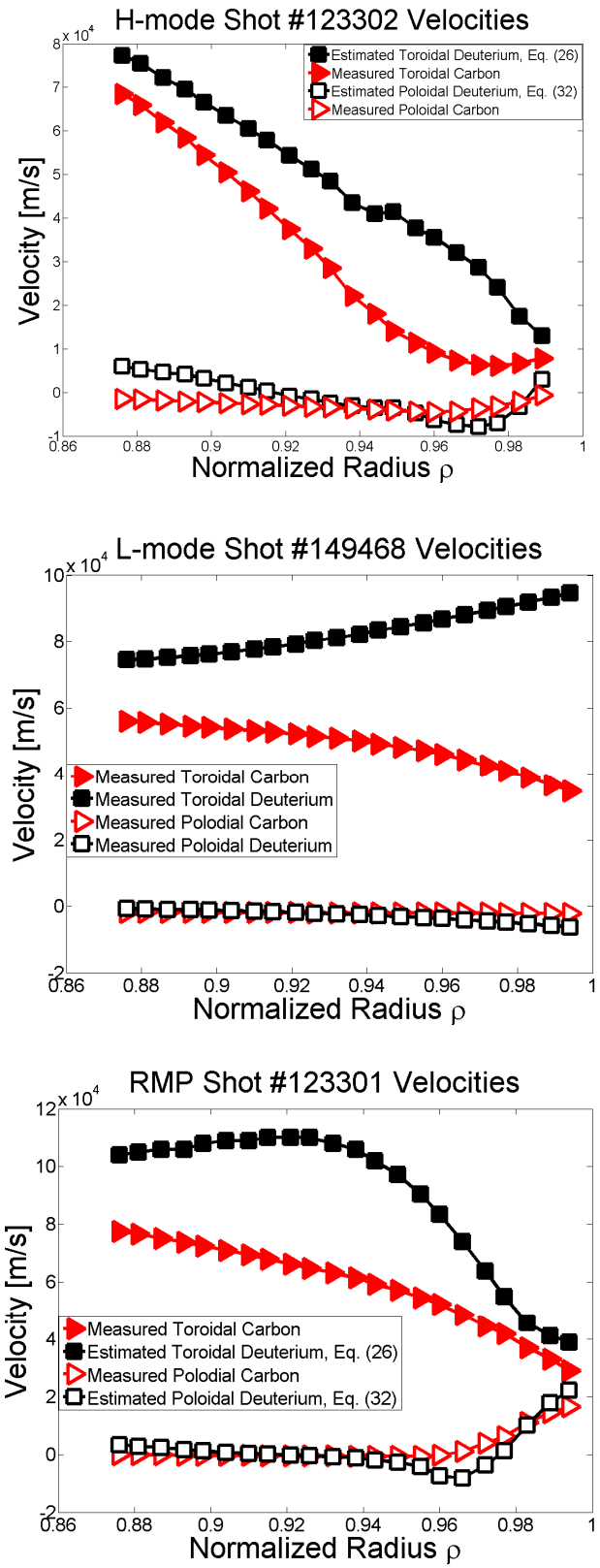

Figure 12: "Experimental" velocities for carbon and deuterium for a) H-mode shot #123302 b) L-mode shot #149468 c) RMP shot #123301.

To reiterate, the deuterium rotation velocities for the H-mode and L-mode discharges are estimated, but the L-mode discharge deuterium velocities are measured.

4.3 Validation of Ohm's Law

Using the estimated deuterium velocities and measured data, the modified Ohm's Law prediction in Eq. (21) can be compared to the experimental radial electric field derived from the carbon radial momentum balance equation, Eq. (16).

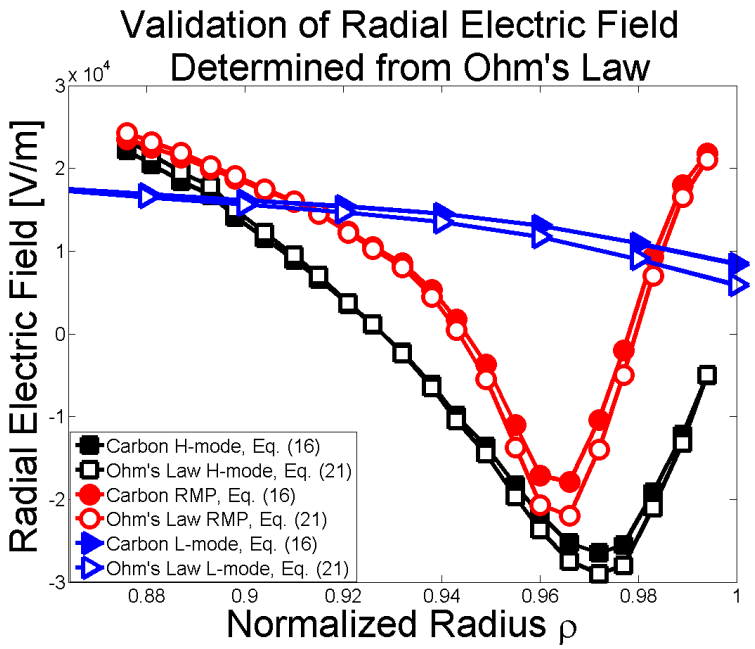

Figure 13: The Ohm's Law (Equation 21) expression for radial electric field agrees with the carbon experimental value (Equation 16) for the three DIII-D test shots.

Figure (13) illustrates that the radial electric field in the edge pedestal region can be calculated using the modified Ohm's Law for various operating regimes, provided that correct values for the rotation velocities are used. Calculations for all three discharges capture the correct structure of the electric field, while exhibiting only slight errors in magnitude. These small errors are thought to arise from small uncertainties in the velocity

profiles. This agreement over a range of operating regimes is considered a validation of the Ohm's Law expression for E_r given by Eq. (21).

Figure (14) compares the contributions from the experimental toroidal velocity, poloidal velocity, and pressure gradient terms in Eq. (21) for the H-mode shot. Note that each component accounts for the contribution from both the carbon and deuterium species.

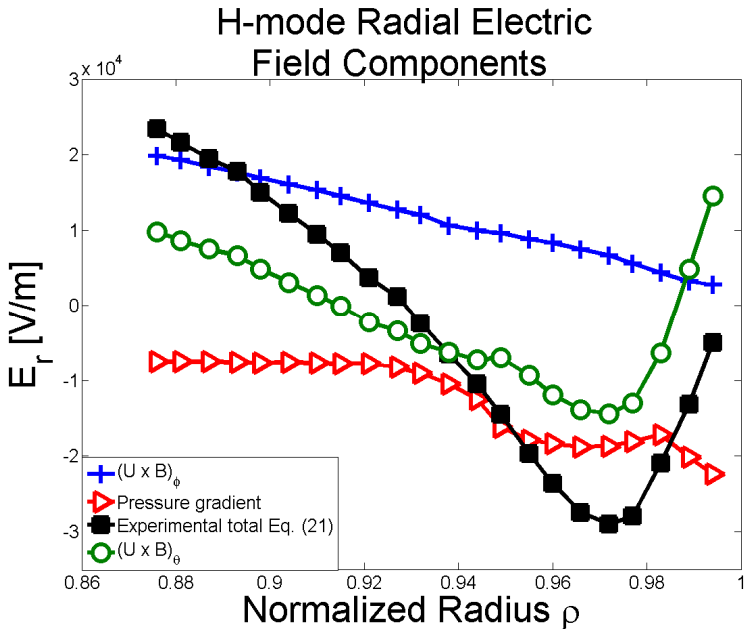

Figure 14: Pressure and motional components of radial electric field calculated by the modified Ohm's Law equation.

For this H-mode discharge, the deep "well" characteristic of typical RMP and H-mode shots is correlated with the poloidal velocity profiles for both species used in the modified Ohm's Law calculation of Eq. (21), while the pressure gradient contribution acts to shift the entire profile in the negative direction. While it is generally accepted [74] that the radial electric field component due to the pressure gradient is important, this result illustrates the importance of the radial electric field component produced by a rotating plasma, or the "motional" electric field, which emphasizes the requirement that

analytical models for the toroidal and poloidal velocities are required for both species. Similar results for the role of the motional radial electric field have also been characterized for B^{5+} and He^{2+} plasmas [74], and well as the RMP discharge discussed in this work.

CHAPTER 5

PREDICTIVE ROTATION THEORY

With the modified Ohm's Law expression for E_r successfully validated in Chapter 4 by comparison with experiment when using experimentally determined velocity profiles, the development of a first principles calculation for E_r requires a first principles model for toroidal and poloidal velocities in the edge plasma. Representative theoretical models, which are consistent with the momentum balance models used previously, are assembled from literature and compared with DIII-D measurements. The predictive analysis presented will focus on the H-mode shot #123302 due to emphasized kinetic effects as compared to the L-mode discharge, and decreased fluctuations from magnetic perturbations compared to the RMP discharge.

5.1 Toroidal Velocity

The toroidal momentum balance from Eq. (11) for both species can be simultaneously [52,66] solved for $V_{\phi j/k}^{fluid}$. The experimental velocity predictions is then obtained from Eq. (24).

$$V_{\phi j}^{exp} = \frac{\left[\frac{e_j B_\theta \hat{\Gamma}_{rj} + M_{\phi j} + n_j e_j E_\phi}{n_j m_j (\nu_{jk} + \hat{\nu}_{dj})}\right] + \frac{\nu_{jk}}{\nu_{jk} + \hat{\nu}_{dj}}\left[\frac{e_k B_\theta \hat{\Gamma}_{rk} + M_{\phi k} + n_k e_k E_\phi}{n_k m_k (\nu_{kj} + \hat{\nu}_{dk})}\right]}{1 - \frac{\nu_{jk}\nu_{kj}}{(\nu_{jk} + \hat{\nu}_{dj})(\nu_{kj} + \hat{\nu}_{dk})}} + \Delta V_{\phi j}^{IOL} \quad (33a)$$

$$V_{\phi k}^{exp} = \frac{\left[\frac{e_k B_\theta \hat{\Gamma}_{rk} + M_{\phi k} + n_k e_k E_\phi}{n_k m_k (\nu_{kj} + \hat{\nu}_{dk})}\right] + \frac{\nu_{kj}}{\nu_{kj} + \hat{\nu}_{dk}}\left[\frac{e_j B_\theta \hat{\Gamma}_{rj} + M_{\phi j} + n_j e_j E_\phi}{n_j m_j (\nu_{jk} + \hat{\nu}_{dj})}\right]}{1 - \frac{\nu_{jk}\nu_{kj}}{(\nu_{jk} + \hat{\nu}_{dj})(\nu_{kj} + \hat{\nu}_{dk})}} + \Delta V_{\phi k}^{IOL} \quad (33b)$$

Equations (33) involve similar parameters to those described in Chapter 3 of this paper, with ion orbit loss accounted for in the radial particle flux, $\hat{\Gamma}_{rj}$, and the viscous

drag frequencies, $\hat{\nu}_{dj/k}$. The net carbon radial particle flux, $\hat{\Gamma}_{rk}$, is set to zero in this calculation based on the argument that the inward flux due to sputtering and recycling must be equal to the outward flux in equilibrium with no internal source.

The structure of the toroidal velocity profiles is determined by the two drive terms for deuterium and carbon, which are proportional to momentum transfer frequencies, and comprised of radial particle flux, external momentum, and induced toroidal electric field terms. Ion orbit particle loss affects the radial particle flux in both the IOL1 and IOL2 calculations shown in Fig. (15). Additionally in the IOL2 calculation, ion orbit momentum loss produces intrinsic rotation added to the fluid toroidal velocity. The viscous drag frequencies for the H-mode discharge is inferred from perturbation theory as described in Eqs (28-30). Figure (15) compares the calculated velocities of Eqs. (33) with the experimentally measured velocities for carbon and the calculated perturbation theory velocity profiles for deuterium, as well as the effects of intrinsic rotation on the calculation.

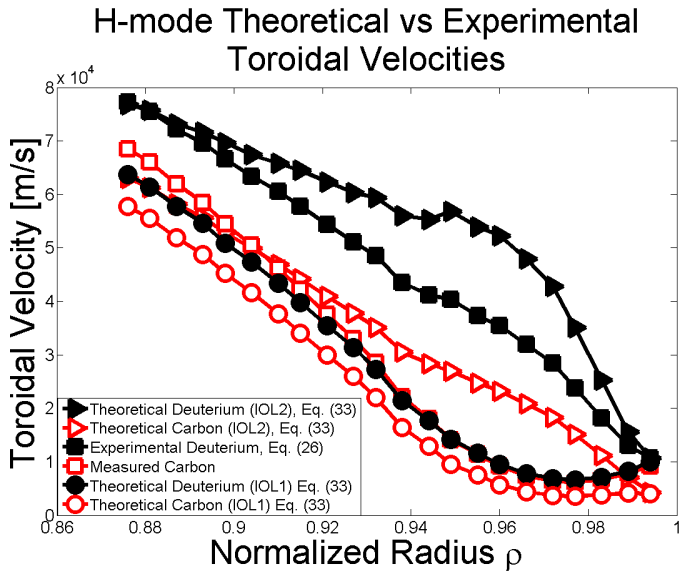

Figure 15: Comparison of theoretical and experimental toroidal rotation velocities for H-mode discharge #123302. (IOL1 includes particle ion orbit loss and IOL2 includes both particle and momentum ion orbit loss.)

The predictive toroidal velocity results with ion orbit particle loss (IOL1) corrections in Fig. (15) show reasonable agreement with experiment. However, the toroidal velocities further corrected for ion orbit loss momentum loss by an intrinsic rotation correction (IOL2) show somewhat poorer agreement. This result is attributed to the ad hoc formalism for intrinsic rotation, used in conjunction with perturbation theory, to estimate the deuterium drag frequencies.

5.2 Poloidal Velocity

The poloidal momentum balance equation can be written for both species using the Stacey-Sigmar form for parallel viscosity [68,75] in an axi-symmetric plasma with an external momentum source due to ion orbit loss [52], using the definition for momentum source $M_{\theta j}$ due to IOL defined in Eq. (15).

$$\left(\nu_{visc,j} + \nu_{jk} + \nu_{atom,j}\right)V_{\theta j} - \nu_{jk}V_{\theta k} = -B_\phi\left(\frac{e_j}{n_j m_j}\hat{\Gamma}_{rj} - \nu_{visc,j}\frac{K^j T_j L_{T_j}^{-1}}{e_j B^2}\right) + M_{\theta j} \qquad (34)$$

Where $\nu_{visc,j} = qf_j V_{th,j}/R$, $f_j = \epsilon^{-\frac{3}{2}}\nu_{jj}^*\left(1+\epsilon^{-\frac{3}{2}}\nu_{jj}^*\right)\left(1+\nu_{jj}^*\right)$, $\nu_{jj}^* = {\nu_{jj}qR}\big/{V_{th,j}}$, and the Hirshman-Sigmar coefficients [76-78] are used to define $K^j = {\mu_{01}^j}\big/{\mu_{00}^j}$. The two momentum balance equations can be solved simultaneously for $V_{\theta j/k}$ and with the momentum source written explicitly from Eq. (15) to yield the predictive model expressions which are dependent upon the poloidal ion orbit loss intrinsic rotation, ΔV_θ^{IOL}.

$$V_{\theta j} = \frac{-B_\phi/\nu_{\theta j}\left[\left(\nu_{visc,j}\frac{K^j T_j}{e_j B^2}L_{T_j}^{-1} + \frac{e_j}{n_j m_j}\hat{\Gamma}_{rj}\right) + \frac{\nu_{jk}}{\nu_{\theta k}}\left(\nu_{visc,k}\frac{K^k T_k}{e_k B^2}L_{T_k}^{-1} + \frac{e_k}{n_k m_k}\hat{\Gamma}_{rk}\right)\right]}{\left(1 - \frac{\nu_{jk}\nu_{kj}}{\nu_{\theta j}\nu_{\theta k}}\right)} + \Delta V_{\theta j}^{IOL} \quad (35a)$$

$$V_{\theta k} = \frac{-B_\phi/\nu_{\theta k}\left[\left(\nu_{visc,k}\frac{K^k T_k}{e_k B^2}L_{T_k}^{-1} + \frac{e_k}{n_k m_k}\hat{\Gamma}_{rk}\right) + \frac{\nu_{kj}}{\nu_{\theta j}}\left(\nu_{visc,j}\frac{K^j T_j}{e_j B^2}L_{T_j}^{-1} + \frac{e_j}{n_j m_j}\hat{\Gamma}_{rj}\right)\right]}{\left(1 - \frac{\nu_{kj}\nu_{jk}}{\nu_{\theta k}\nu_{\theta j}}\right)} + \Delta V_{\theta k}^{IOL} \quad (35b)$$

The poloidal composite momentum transfer frequency, $\nu_{\theta j} = \nu_{visc,j} + \nu_{atom,j} + \nu_{jk} + \nu_{anom\theta,j}$, depends on poloidal viscosity, atomic physics, interspecies collisions and anomalous transport processes.

Comparing the theoretical poloidal velocity models with experiment for the H-mode discharge, Fig. (16) again shows order of magnitude agreement in profile trends, but some difference in specific profile structure. Inclusion of intrinsic rotation improves the agreement of prediction with experiment in this case.

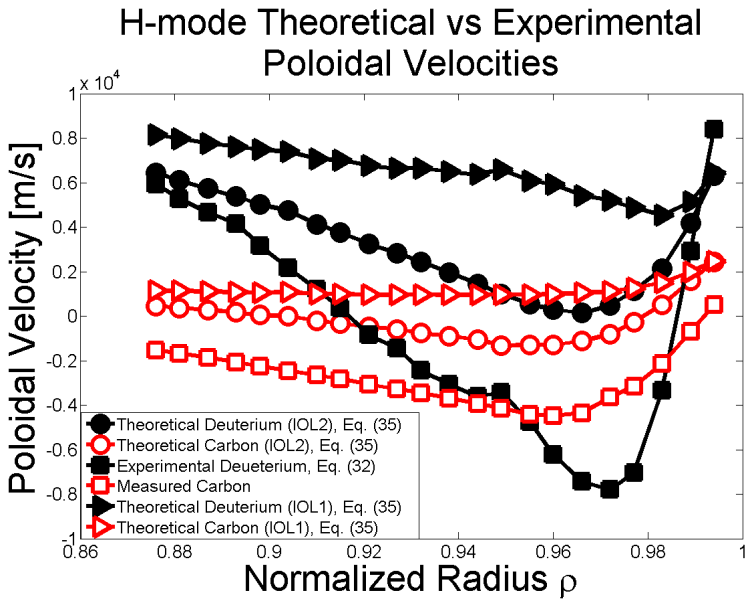

Figure 16: Comparison of theoretical and experimental poloidal rotation velocities for H-mode discharge #123302. (IOL1 includes particle ion orbit loss and IOL2 includes both particle and momentum ion orbit loss.)

Because of a preferential loss of particles in the counter current direction, it is seen in Fig. (15) that the toroidal velocity increases in magnitude because of intrinsic rotation. However, Fig. (16) shows the poloidal velocity decreases with intrinsic rotation due to the helicity of the magnetic field lines in a tokamak with the plasma current in the opposite direction to the toroidal magnetic field, which is the case for this H-mode

discharge (as well as the RMP and L-mode shots considered). The negative contribution of ion orbit loss to the poloidal velocity along with the negative pressure gradient term is what characterizes the negative "well" structure of the radial electric field. In contrast to the calculated toroidal velocity, the inclusion of ion orbit momentum loss (in the form of an intrinsic rotation correction, IOL2) yields enhanced agreement to experiment for the poloidal velocity calculation.

CHAPTER 6

IMPROVEMENTS TO STANDARD ION ORBIT LOSS THEORY

The predictive neoclassical rotation models, and hence the radial electric field calculation, depend heavily on the ion orbit loss formalism and means of evaluation. Therefore, several steps are made to improve upon the "standard" theory for the minimum ion energy at which IOL occurs [10], overviewed in Chapter 3, to include losses of fast neutral beam ions and the use of experimental parameters to construct flux surfaces instead of assuming a flux conserved circular geometry.

6.1 Fast Neutral Beam Ion Orbit Loss

Fast ions are accelerated to roughly 80keV, converted into neutral molecules of D_1, D_2, or D_3, and are then launched into the DIII-D plasma for heating, current drive, and rotational drive. Since there are several molecules of deuterium, the neutral beam takes three characteristic energies: full energy E for D_1 molecules, half energy E/2 for D_2 molecules, and third energy E/3 for D_3 molecules, where E is the acceleration energy. The fraction of the total beam in each energy component has been experimentally determined and can be calculated as a function of the total energy component [79]. For this analysis, the fraction of injected beam particles is approximately 76%, 13%, and 11% for the full, half, and third energy components, respectively.

The neutral molecules are deposited on flux surfaces via processes like charge exchange and ionization. Fast ion deposition profiles, shown in Fig. (17a), can be calculated using various numerical codes such as NUBEAM [79] and NBeams [65].

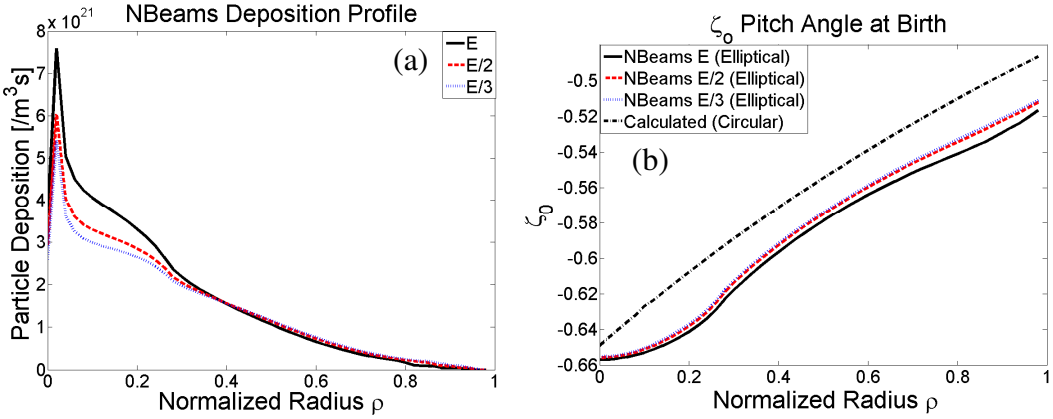

Figure 17: a) Neutral beam deposition profiles calculated from NBeams for each energy component b) Pitch angle comparisons for elliptical flux surfaces calculated by NBeams and circular flux surfaces.

The DIII-D tokamak has four neutral beam injection ports, three of which are positioned for co-current injection. Since each beam follows a straight-line deposition trajectory defined by the unit vector $\hat{\ell}$, there is a characteristic angle of the beam direction with respect to the toroidal magnetic field, called the pitch angle, $\zeta_0 = \hat{\ell} \cdot \vec{B}/B$. Figure (17b) shows the pitch angle calculated for circular flux surfaces compared to elongated elliptical flux surfaces generated from NBeams ($\zeta_0 > 0$ for ctr-I, $\zeta_0 < 0$ for co-I ions). The elliptical pitch angles were used for the ion orbit loss calculations in this dissertation.

The ion orbit loss calculation for fast ions can be derived by treating the pitch angle and velocity distribution differently than was previously discussed for the thermal population. The minimum energy calculation from Eq. (4) takes the pitch angle in as a dependent variable. (For thermal ions, particle trajectories can have any angle with respect to the toroidal magnetic field, therefore all pitch angles were considered.) The fast ion calculation requires only one pitch angle for each surface as required by geometry. This simplification allows the minimum energy calculation to solely depend on the

poloidal angle, instead of both the poloidal angle and the toroidal angle as is the case for thermal ions.

Furthermore, the beam energy distribution function is assumed to be a delta function centered around three specific energies derived from the injection system, as opposed to a Maxwellian distribution as in the thermal ion case. The neutral beam injection (NBI) system can be seen as a mono-energetic external source of particles with a single pitch angle onto flux surfaces. If minimum energies for each flux surface are calculated, then the fast loss fraction simply depends on whether the NBI energy component exceeds the minimum energy requirement for the flux surface on which the beam is ionized for the ions to be ion orbit lost. Fast ions which are promptly lost due to IOL affect the continuity equation in the same way as thermal losses, except that they are applied to decrease the NBI source term instead of the particle flux as a whole. The deposition profile is used to modify the NBI source term for the continuity equation to look like Eq. (36).

$$\hat{S}_{nbi} = \sum_{i=1}^{3} \frac{P_{beam}}{E_{beam}^{i}} \left[1 - 2f_{fast}^{IOL,i}(\rho)\right] H^{i}(\rho) \tag{36}$$

H is the neutral beam deposition profile calculated from NBeams and shown in Fig. (17a). The NBI source rate is summed over all the energy components, where the particle energy, loss fraction, and the deposition profile structure is dependent upon the energy component, *i*, representing *E*, *E*/2, and *E*/3. The fast ion loss fraction is calculated by considering the number of poloidal loss directions for all energy components on each flux surface divided by the total number of poloidal directions.

$$f_{fast}^{IOL}(\rho) = \sum_{i=1}^{3} f_{fast}^{IOL,i} = \sum_{i=1}^{3} \frac{\int_0^{\pi} \theta \in E_{min}^{i}(\rho,\theta) < E_{nbi}^{i}\, d\theta}{\int_0^{\pi} \theta\, d\theta} \tag{37}$$

The condition $\theta \in [E^i_{min}(\rho,\theta) < E^i_{NBI}]$ requires fast neutral beam ions to have greater energy than the minimum needed for ion orbit loss to be included in the integral.

The inward return current compensating the loss of fast ions is assumed to consist of thermalized ions from the scrape off layer, accounting for the factor of 2 in the thermal ion radial particle flux source of Eq. (9). While the thermal ion loss fraction of Eq. (5) is cumulative in radius, the fast beam ion loss fraction of Eq. (37) is differential at the local radius.

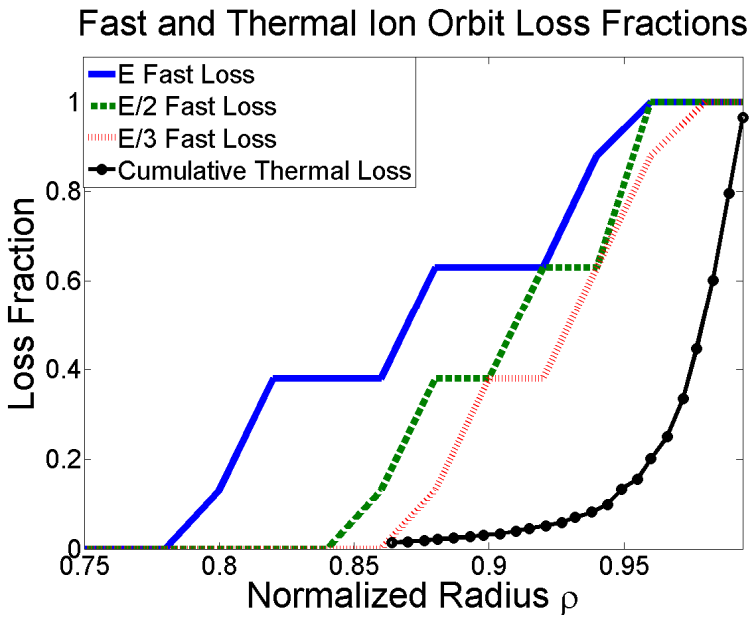

Figure 18: Ion orbit loss fractions for fast neutral beam particles of different energy components and for thermal ions.

Figure (18) shows the loss fractions for the various energy components of fast beam ions compared to the cumulative (in radius) thermalized ion loss fractions calculated from Eq. (37) and (5), respectively. The "stair-step" profile structure of the fast ion loss fractions is due to the small number of poloidal loss angles considered numerically, which can be readily extended in future analysis. The fast loss profiles extend farther into the plasma than the thermal loss profiles, suggesting the possibility

that for very high energy NBI systems or systems that focus on injecting particles in the edge where these large NBI loss fractions exist, may generate significant fast losses which would be coupled with large return currents. Substantial fast ion losses in the edge like this have the potential to generate significant intrinsic rotation, and are therefore of great interest for investigations of situations where direct NBI cannot drive rotation in the usual way such as is predicted for ITER [35].

Fast loss fractions often extend farther into the plasma than the region considered for edge calculations in this research. The losses inside of the edge pedestal region shown in Fig. (1) are integrated and removed from the total core NBI source that determines the core boundary condition for the particle flux calculation in the edge region. The edge region fast losses are maintained as a radial function to be included in the edge continuity equation.

6.2 Experimental Flux Surfaces and Magnetic Fields

Previous ion orbit loss models [10] use a simplified circular geometry described in Eq. (22) to calculate flux surface values as well as parameters like magnetic fields and major radii.

$$R(r,\theta) = \bar{R}h(r,\theta) \tag{38a}$$

$$B_{\theta,\phi}(r,\theta) = \bar{B}_{\theta,\phi}h(r,\theta) \tag{38b}$$

$$h(r,\theta) = 1 + \frac{r}{\bar{R}}\cos(\theta) \tag{38c}$$

Ampere's Law has been used in previous calculations, assuming uniform current density, to define flux surface values.

$$\psi = RA_{\phi} = \frac{\mu_0 I \bar{R} r^2}{4\pi a^2} \tag{39}$$

where "I" is the plasma current and "a" is the minor radius.

The minor radius was assumed in previous calculations to be that of the effective circular geometry that preserves the surface area for an elongated elliptical plasma of horizontal dimension 2a and vertical dimension 2b, $\bar{a} = \sqrt{\frac{1}{2}\left(1 + \left({}^{b}/_{a}\right)^{2}\right)}$.

Sensitivity of the calculations of Eqs. (4)-(6) to the flux surface geometry treatment can be explored by comparing the results of calculations using experimental flux surface geometry with calculations using the circular model. Experimental flux surfaces obtained from EFIT [80] are shown in Fig. (19a), and the experimental as well as circular model poloidal magnetic fields in Fig. (19b).

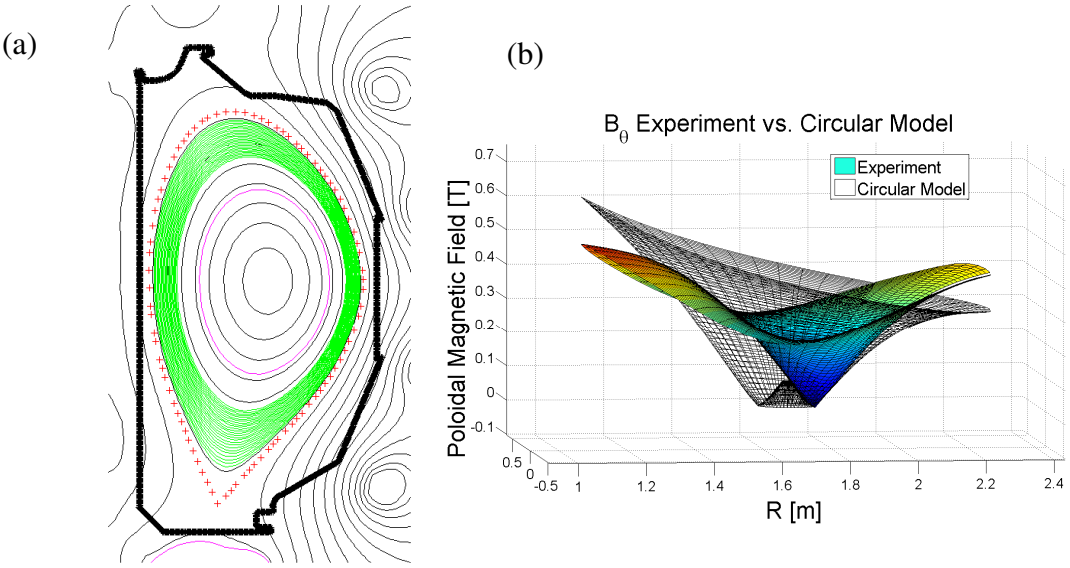

Figure 19: a) Experimental flux surfaces in the edge region (shaded) with the separatrix shown by dotted line b) Experimental poloidal magnetic field (opaque surface) compared to circular model analytical fit (transparent surface).

Experimental data were also used for the toroidal magnetic field, allowing the minimum energy calculation in Eq. (4) to be evaluated with purely experimental parameters. With these model improvements, Fig. (20) shows the influence of flux surface geometry modeling and realistic magnetic fields on the loss fraction calculations.

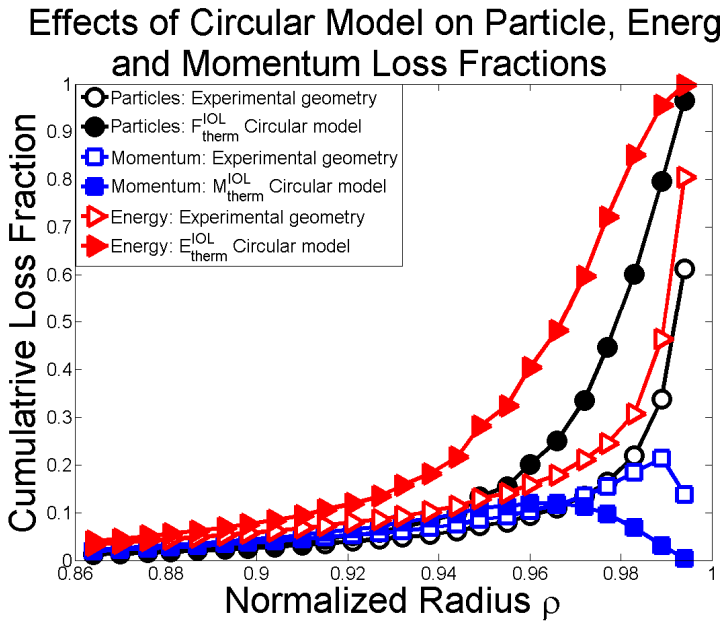

Figure 20: Cumulative ion orbit loss particle, momentum, and energy loss fractions calculated with experimental geometry (empty symbols) and with an effective circular model (solid symbols).

Calculating loss fractions with the experimental flux surface geometry decreases the total cumulative IOL for particles (F_{therm}^{IOL}) and energy (E_{therm}^{IOL}), and changes the structure of the loss profile to show a sharper increase of lost particles in the far edge as opposed to the more gradual loss of particles with the approximate circular model calculation. Momentum losses (M_{therm}^{IOL}) reflect similar results by shifting the larger and more pronounced peak towards the separatrix when using experimental flux surface values as compared to the circular model, which agrees with previous models and experimental observations [39,41,81].

In order to make this improved model predictive, an analytical fit to flux surfaces must be used. Previous analysis [82] has shown that a modified Miller model is an accurate and computationally manageable means to model flux surfaces. The Miller model [83] is an analytical geometric model that can treat elongated plasma geometries

by representing Cartesian (R,Z) coordinates of plasma flux as functions of plasma elongation, κ, and triangularity, δ.

$$R(r,\theta) = R_0 + r\cos\xi \quad (40a)$$

$$Z(r,\theta) = \kappa r \sin\theta_m \quad (40b)$$

Where $\xi(r,\theta) = \theta_m + x_\delta(r)\sin\theta_m$, $x_\delta = \sin^{-1}\theta_m$, and θ_m is slightly different from the true poloidal angle and is defined by the triangle with hypotenuse of κr, and height Z. This model was employed to generate a new mesh with more realistic flux surfaces in the outer plasma region for the ion orbit loss calculation (but not the general plasma balance calculation in GTEDGE). These modeled surfaces shown by the wire mesh in Fig. (21) represent the experimental (green) flux surfaces much more accurately than a circular model, and yield almost identical IOL results (<1% flux surface positional error [82]) as the experimental calculations.

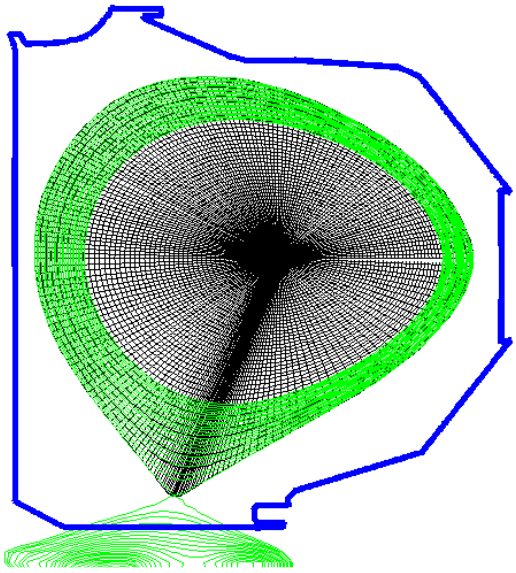

Figure 21: Mesh calculated using the analytical Miller model compared with experimental (green) flux surface geometry, which is used in the ion orbit loss calculation.

The improved flux surface model can be used for both thermal and fast ion loss calculations, then applied to the main GTEDGE calculation via loss fraction profiles so there are no geometric issues with merging the two models.

CHAPTER 7

RETURNING PARTICLES FROM THE SCRAPE OFF LAYER

Particles which satisfy the conservation requirements to be ion orbit lost may return to the plasma after executing those orbits that cross the separatrix into the scrape off layer. If the fraction of this number of returning particles to the total number of particles that satisfy IOL requirements is unity, then no particles are actually ion orbit lost; if it is zero, then all IOL particles are removed from the plasma. In reality, the fraction lies somewhere in between. To investigate this further, the particle following code ORBIT [84] was modified to perform a numerical study tracking particle trajectories outside of the separatrix. It is assumed that if the particle orbit intersects with the vessel wall, then those trajectories are considered absolutely lost, whereas other orbits have the possibility of returning the ions to the plasma. Further analysis is required to extend this simulation to account for processes that are occurring in the SOL such as charge exchange or collisions with neutrals, which would remove particles from the plasma even with trajectories that do not intersect the wall.

For the present study, particles orbits were traced for 104 trial trajectories from each of 90 boundary points along the separatrix, at 5 different energies (100 eV, 500 eV, 1 keV, 3 keV, 5 keV). The 104 different trajectories are shown for one boundary point in Fig. (22), where the (red) trajectories to the left represent particles launched away from the plasma core, and the (blue) trajectories to the right are towards the plasma core. The direction of each trajectory was chosen to sweep all angles with respect to the local toroidal magnetic field.

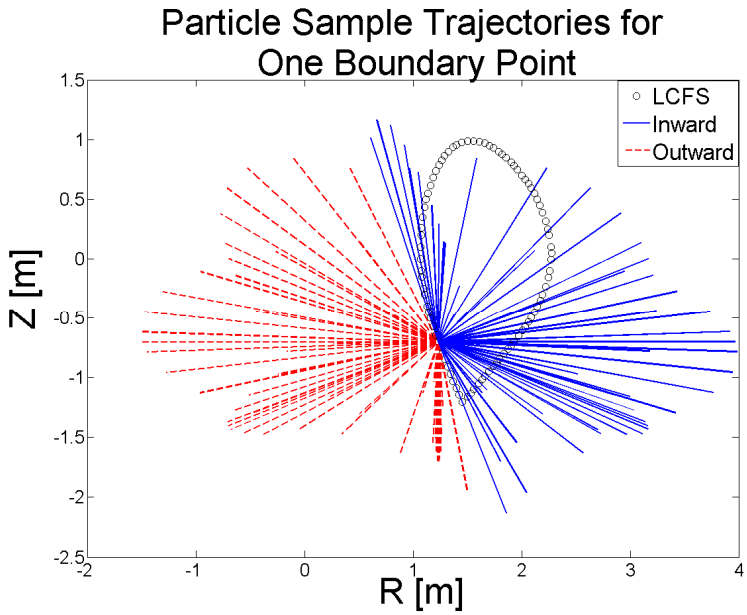

Figure 22: Example of 104 initial velocity vector positions for a single boundary point on the separatrix. Particle trajectories based on these conditions were followed by a Lorentz solver to analyze the fraction of particles that hit the wall. Blue launches are towards the core and red are towards the scrape off layer.

After calculating all the orbits, the fraction of ions that hit the wall was determined as a function of energy, shown in Fig. (23). It is interesting to note that very low energies have a large non-return fraction, then a threshold is reached where the non-return fraction drastically decreases before increasing at a slower monotonic rate through the keV range. The lower energy particle loss with a higher non-return fraction mostly occurs in the upper inboard quadrant. A potential cause for this is due to high energy particles drifting inwardly due to magnetic field curvature from neoclassical drifts, while the lower energy particles do not, and simply strike the wall (which is very close to the plasma in this region).

This analysis shows that roughly 40% of ions that can energetically make it to the separatrix will strike the wall and be removed from the plasma. This fraction will be

considered the “non-return” fraction. Of the other 60%, some may still be removed due to charge exchange or collisions with neutrals, but this must be explored further.

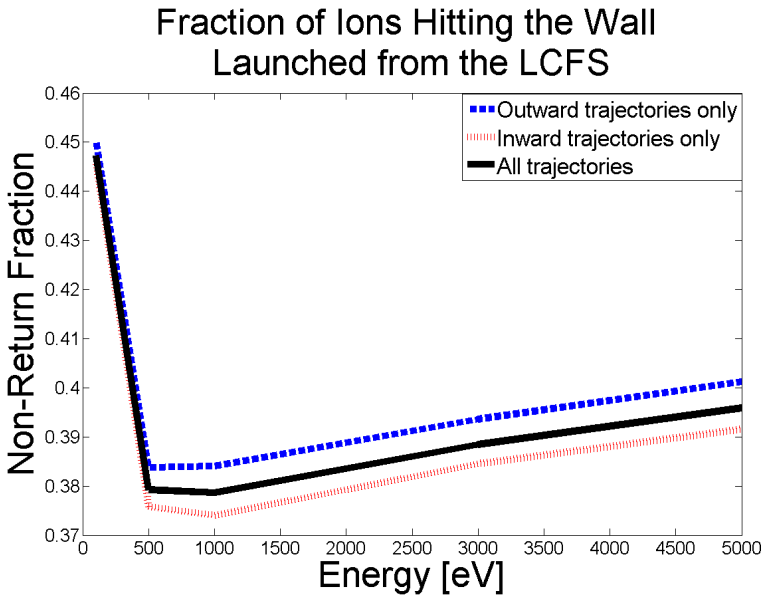

Figure 23: Fraction of ions that hit the wall out of all trajectory trials as a function of energy.

The non-return fractions can also be analyzed as a function of poloidal position, as shown in Fig. (24). There are spikes in fractions of particles striking the wall at the upper chamber wall located approximately at the top of the plasma ($\theta = \pi/2$), outboard midplane ($\theta = 0$), and the divertor ($\theta = 3\pi/2$). Losing particles at the top of the plasma is consistent with the close proximity of the plasma to the chamber wall at this location in DIII-D (see Fig. (21)). Also consistent with losses at $\theta = 0$ and $\theta = 3\pi/2$, previous IOL analysis [50,85] has predicted peaking in lost particles at the outboard midplane and an importance of x-loss [42,53] in the divertor region due to the null in poloidal magnetic field at the x-point.

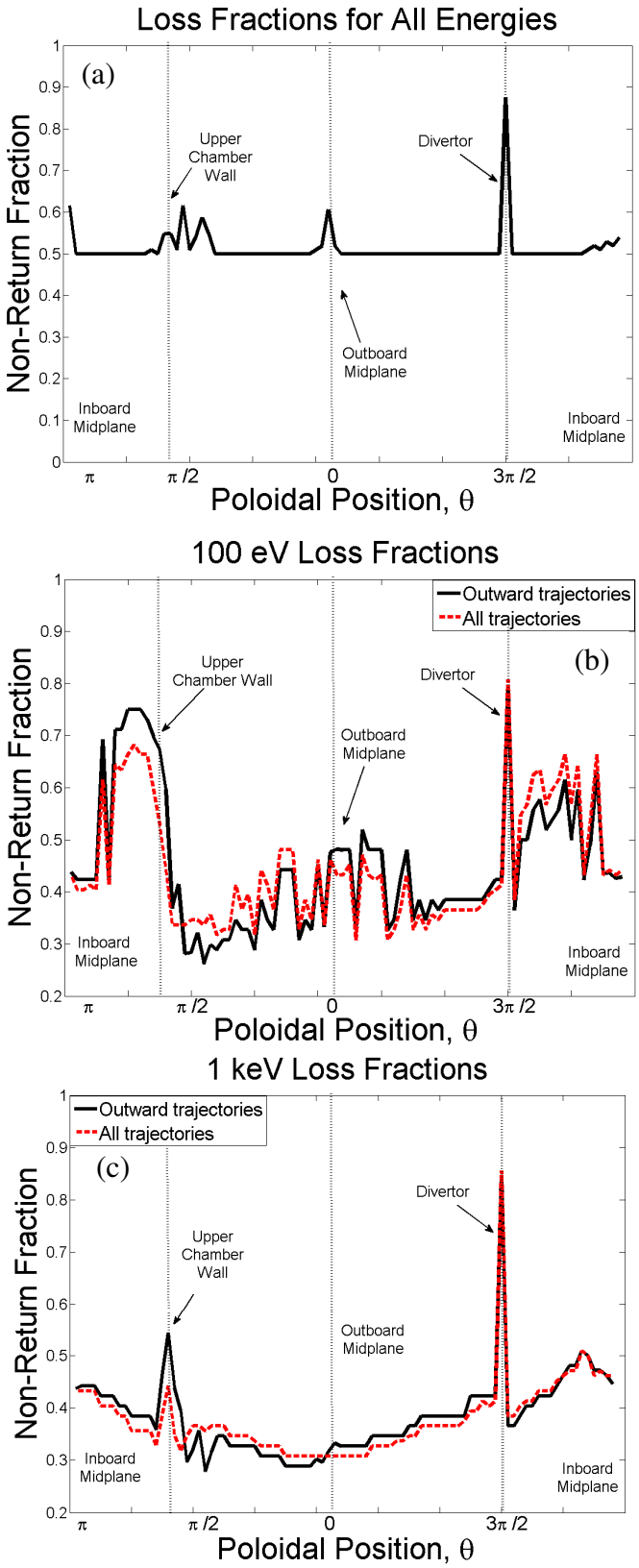

Figure 24: Ion loss fractions as a function of poloidal position for a) all energy outward trajectories b) 100 eV ions c) 1 keV ions.

When analyzing the poloidal dependence of losses at different energies, it is seen that the 100 eV energy ions exhibit larger variations in the non-return fraction than the 1 keV ions. The 1 keV ions have distinct loss peaks for the upper chamber wall and the divertor regions, but appear to have similar loss fractions for the inboard and outboard sides of the plasma. The peak in the low energy non-return fraction in Fig. (23) is explained by the large increase in lost particles shown in Fig. (24b) at the upper chamber wall of the vacuum vessel. These low energy ions do not have enough kinetic energy to neoclassically drift back into the plasma, and strike the wall which is very close to the last closed flux surface at this poloidal location.

A similar analysis was performed for fast beam ions, but instead of launching particles from the separatrix, particle tracking was initiated along the outboard midplane, where the neutral beams are injected. Results showed that >90% of fast beam particles that are energetically allowed to execute IOL orbits will hit the wall; therefore the fast fraction remains essentially unchanged.

An interesting outcome of this simulation was that fast ions began striking the wall (i.e. being ion orbit lost) in the ORBIT numerical Lorentz force simulation at the same launch radius ($\rho \approx 0.7$) for which the modified circular model first calculated NBI fast ion losses in Fig. (4) from conservation principles, validating this part of the fast beam IOL calculation.

CHAPTER 8

X-TRANSPORT AND X-LOSS

Another non-diffusive transport mechanism considered is called X-transport [42,53]. There is a region near the divertor x-point where the poloidal magnetic field becomes very small, shown in Fig. (25). In this region, the particle transport is different than in the rest of the plasma because the only magnetic field is in the toroidal direction, constraining particles to travel only in the toroidal direction with negligible poloidal displacement. Because the ions are not rotating poloidally, there are no neoclassical cancellations of velocity drifts, which allow ions to possibly drift out of the plasma through the x-point before exiting this x-region. This was seen in the Lorentz force particle orbit simulation in the previous section by the spike in lost particles at $\theta=3\pi/2$ in Fig. (24).

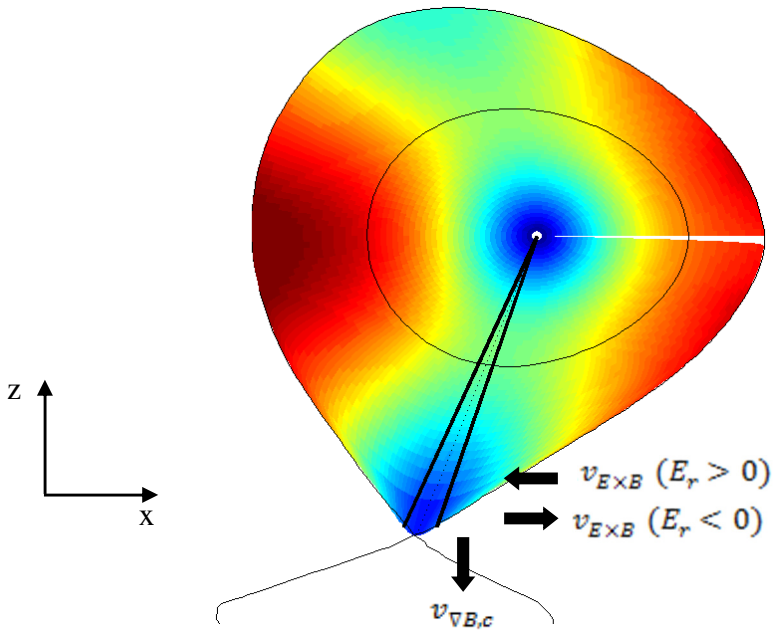

Figure 25: Schematic of the x-region near the x-point showing drift directions. Colored background represents the poloidal magnetic field, with the small B_θ regions in dark blue.

The particle transport in this region is dominated by a) poloidal $E_r x B_\varphi$ drift and b) vertically downwards curvature and grad-B drifts, which are described by Eq. (41)-(43).

$$\vec{v}_{E\times B} = \frac{\vec{E}\times\vec{B}}{B^2} = \frac{E_r}{B_\phi}\hat{n}_\theta \tag{41}$$

$$\vec{v}_{\nabla B} = \frac{W_{perp}\vec{B}\times\nabla B}{eB^3} = \frac{W_{perp}}{eB_\phi^2}\frac{\partial B_\phi}{\partial R}\,\hat{n}_z \tag{42}$$

$$\vec{v}_c = -\frac{W_{par}\vec{B}\times\hat{n}_x}{eB^2R} = \frac{2W_{par}}{eB_\phi R}\,\hat{n}_z \tag{43}$$

W is the ion energy in the parallel or perpendicular direction. During the time that the particle is inside the x-region, there is competition between these two drifts to transport the particle poloidally back into the plasma, x-transport to a different flux surface, or x-loss out of the plasma entirely. If the poloidal drifts are sufficiently small, the ion will drift vertically downward across the separatrix through the x-point and be x-lost. In the far edge region where the radial electric field changes sign, the poloidal drift is reversed in direction, allowing longer time periods for particles to be x-transported or x-lost due to the grad-B and curvature drifts. If the poloidal ExB drift is dominant, then the ions will remain in the plasma but be x-transported to a flux surface closer to the separatrix.

Large scale Monte Carlo guiding center simulations have identified x-loss as a dominant source of non-ambipolar ion transport, and therefore an agent of a radial electric field generation in the edge region [42]. Previous models have developed x-transport theory with averaged time scales over the entire x-region using a modified circular model [53]. This research aims to extend the modified circular model theory by incorporating realistic geometry and particle tracking to determine realistic minimum energy values required for particles to be x-transported from an inner flux surface to each outer flux surface. Similar to ion orbit loss theory, minimum energy matrices for ions to

be x-transported or x-lost can be used to develop a methodology for incorporating the non-diffusive transport mechanisms into edge fluid models.

The previous modified circular model [53] can be used to calculate the minimum energy required to x-transport ions from an inner flux surface to an outer flux surface using Eq. (44) as a constraint and assuming that ions with greater energy than the minimum energy, $W_{min}^{x}(n \rightarrow m)$ can also be transported just as far across flux surfaces.

$$W_{min}^{x}(n \rightarrow m) = \frac{\Delta r_{n \rightarrow m} eRE_{rn}}{r_n \Delta\theta_x \left(1+\xi_0^2\right)} \tag{44}$$

The x-region has poloidal arc width, $r\Delta\theta_x$, and is divided into radial segments of width $\Delta r_{n \rightarrow m}$between flux surfaces n and m, traveling in direction $\xi_0 = \cos\left(\frac{V}{V_{\|}}\right)$ with respect to the magnetic field. This simplified circular model, whose geometry is illustrated in Fig. (26), will be used as a comparison to a more in depth particle tracking method developed for this research.

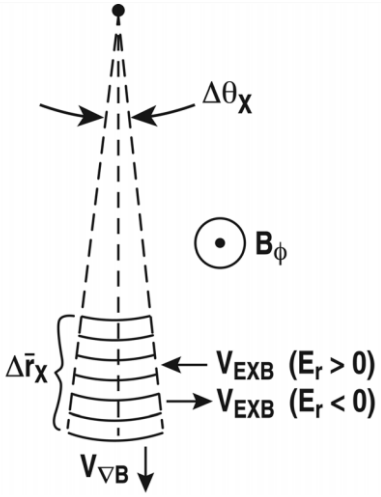

Figure 26: Schematic of simplified circular model geometry for x-transport calculation. (Reproduced from reference 53 with permission.)

Extended x-transport methodology includes calculating the velocity field from the poloidal and vertically downward drifts, then tracking ion trajectories through the x-

region due to the experimental magnetic field and radial electric field distributions. Particles that begin on flux surfaces on the left side of the x-region, as in Fig. (27), are moving in the co-current direction. Conversely ions are moving in the counter-current direction if they enter on the right side of the region. The poloidal ExB drift is dominant until the radial electric field approaches zero, then the downward grad-B and curvature drifts have a greater effect. These downward drifts are the primary mechanism for x-transport to occur, however the radial electric field becomes larger in magnitude at a rate rapid enough to keep some x-transported particles in the plasma instead of being lost through the x-point. This process can be assumed to be cyclical in the sense that when no E_r shear is present, ions are easily x-lost, which acts to construct an E_r "well" whose shear constrains more x-transported ions to the plasma. In steady state, there will be a constant x-transport and x-loss associated with a particular E_r whose losses will be determined by the time scale of processes determining E_r and the compensating return currents.

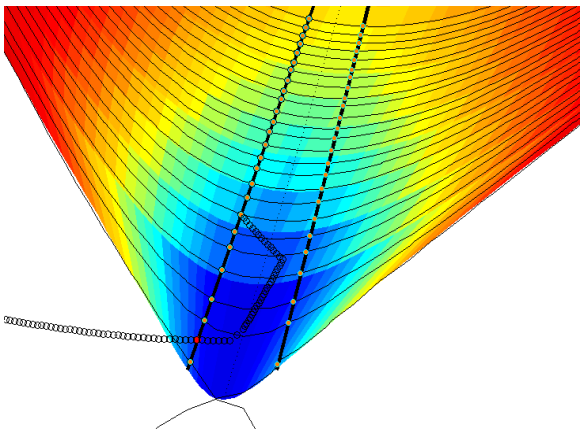

Figure 27: The x-region of the tokamak showing a representative particle trajectory through the region. The dark blue region represents the nulled poloidal magnetic field.

Using this model, a minimum energy matrix similar the previous simplified geometry model in Table 1 of Reference 53 can be calculated describing how much energy is required for a particle on a given inner flux surface to be x-transported to a

given outer flux surface, or out of the plasma entirely. After analyzing x-transport for particles with pitch angle $\xi_0 = \pm 0.5$, results showed that even with extremely high energies up to 20keV, particles were consistently x-transported, but not x-lost out of the H-mode DIII-D plasma, similar to the example trajectory in Fig. (27). Table 2 shows the corresponding minimum x-transport energy matrix for an ion to travel from one flux surface to another in the edge plasma for DIII-D H-mode shot #123302 and $\xi_0 = \pm 0.5$. The format for data presentation in the table is: (modified circular model)/(particle tracking model). For example, according to Table 2, the minimum energy required for an ion to be x-transported from $\rho=0.926$ to $\rho=0.932$ is 0.5 keV for simplified circular model and 0.4 keV for the particle tracking model.

Table 2: Minimum energy matrix for an ion to be x-transported from one flux surface to another. Data format is: (Simplified Geometry Model)/(Particle Tracking Model). Energies are in keV.

ρ	0.932	0.938	0.943	0.949	0.955	0.960	0.966	0.972	0.977	0.983	0.989	0.944	1.00
0.926	0.5/0.4	1.4/1	2.5/X	4.0/X	5.8/X	8.0/X	10.4/X	13.2/X	16.2/X	19.4/X	>20/X	>20/X	>20/X
0.932		0.9/X	2.0/X	3.5/X	5.3/X	7.5/X	9.9/X	12.7/X	15.8/X	18.9/X	>20/X	>20/X	>20/X
0.938			1.1/4.1	2.7/8.0	4.5/>20	6.6/X	9.1/X	11.9/X	14.9/X	18.0/X	>20/X	>20/X	>20/X
0.943				**1.6/3.5**	**3.4/16**	**5.5/>20**	**8.0/X**	**10.8/X**	**13.8/X**	**16.9/X**	**>20/X**	**>20/X**	**>20/X**
0.949					1.9/12.2	4.0/>20	6.5/X	9.2/X	12.3/X	15.4/X	18.6/X	>20/X	>20/X
0.955						2.2/10.7	4.7/>20	7.4/X	10.5/X	13.6/X	16.8/X	19.7/X	>20/X
0.960							2.5/13.8	5.3/>20	8.3/X	11.5/X	14.6/X	17.5/X	20.0/X
0.966								2.8/16.7	5.9/>20	9.0/X	12.2/X	15.0/X	17.6/X
0.972									3.1/14.5	6.2/>20	9.4/X	12.2/X	14.8/X
0.977										3.2/15.6	6.3/>20	9.2/X	11.7/X
0.983											3.2/13.4	6.1/>20	8.6/X
0.989												2.9/10	5.4/>20
0.944													2.6/13

The minimum energy for the simplified geometry model is seen to monotonically increase for an ion to move farther out in the plasma and minimum energy values can be calculated for all combinations of flux surfaces leading to an upper triangular matrix. This assumes a constant radial electric field within the mesh of the calculation. The particle tracking calculation accounts for a varying radial electric field across the ion trajectory. With the inclusion of this physics, the minimum energy matrix takes a diagonal form, suggesting that ions can primarily be x-transported to the n+1 flux surface and results in larger minimum energies to be x-transported in general. This result is consistent with the findings that x-loss, or the particle crossing the separatrix from this mechanism, occurs less frequently than a particle being x-transported to a flux surface closer to the separatrix.

The gray row in Table 2 represents the flux surface where the radial electric field changes from positive to negative. When $E_r=0$, there is no poloidal transport possible in the particle transport model, so particles are not able to enter the x-region, which is why there are no minimum x-transport energies available on this flux surface for the particle tracking model. However, in reality, ions with some poloidal inertia will transport into the x-region on this flux surface and experience an uncontested vertically downwards grad-B drift, which will produce a large source of particles onto the flux surfaces outwardly adjacent to the flux surface where $E_r=0$. The yellow diagonal line represents the most energetically favorable x-transport scenario for an ion to travel from flux surface n to n+1, and will subsequently be used in the fluid model.

Since particles are only energetically allowed to be x-transported one flux surface at a time towards the separatrix like a cascade, when an ion exits the x-region after being

x-transported and re-renters the region of the tokamak with normal neoclassical transport occurring, it is swept around the flux surface and samples all possible locations and minimum energies for ion orbit loss. This process puts conventional ion orbit loss in direct competition with x-transport for each flux surface. The process that has the smallest energy allowing an ion to be transported either out of the plasma (IOL) or to the next flux surface (x-transport) will dictate the loss on that flux surface. To analyze which mechanism dominates, Fig. (28) shows a comparison of minimum energies for x-transport calculated from the particle tracking model and thermal ion orbit loss for edge plasma flux surfaces.

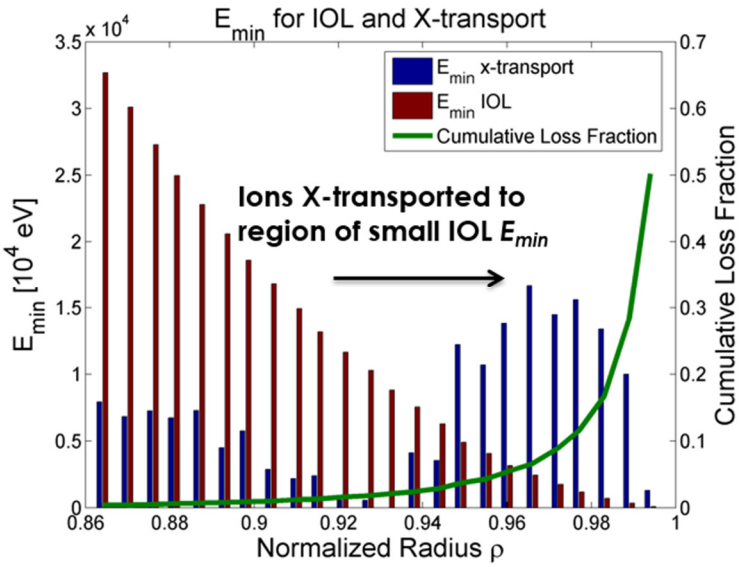

Figure 28: Comparison of minimum energy for co-current particles to be either x-transported or thermally ion orbit lost for a pitch angle of ξ_0 = -0.5.

The minimum energy for thermal IOL is seen to monotonically decrease towards the separtrix. The minimum energy for IOL drops below that of x-transport at ρ=0.943, making IOL more favorable in the outer edge region and x-transport more favorable in the inner edge region. This process of "x-transport pumping" causes lower energy particles in the inner edge region (that were previously not energetically available to be

IOL) to be pumped into a region where they are energetically allowed to be IOL. The unshaded bold row in Table 2 shows the flux surface where IOL becomes dominant. It can be seen that the minimum energies for x-transport become significantly larger for the particle tracking scheme at larger radii than this flux surface compared to the modified circular model. This suggests that any model considering both IOL and x-transport processes must consider them as coupled.

To be incorporated into the fluid equations, the mechanism for making up the lost charge from x-transport and its relationship with conventional IOL must be analyzed. Both IOL and x-transport act on the same ion velocity distribution on a given flux surface. However, there will be an extra source and sink due to x-transport for particles on each flux surface, as indicated in the continuity balance equation.

$$\nabla \cdot \Gamma_{\mathrm{m}} = n_m \nu_{ion,m} + \hat{S}_{nbi,m} - 2\Gamma_{\mathrm{rj,m}} \frac{\partial F_{therm,m}^{IOL}}{\partial r} + \sum_n F_x(n \to m)\Gamma_{rj,n} - \sum_{n'} F_x(m \to n')\Gamma_{rj,m} \quad (45)$$

$F_x(n \rightarrow m)$, which is applied to the radial particle flux on the initial flux surface n, is the loss fraction due to x-transport from flux surface n to flux surface m defined by taking the integral of velocity space similar to the IOL loss fraction from Eq. (5). When using the assumption that ions can only be x-transported across one surface, this sum will disappear and turn into a source from just the previous flux surface. The x-transport sink is similarly defined for the loss of particles on flux surface m due to x-transport to flux surface n' closer to the separatrix. In this continuity equation, either the thermal IOL sink or the x-transport sink apply depending on which process has the most favorable minimum energy.

To simplify this equation for realistic implementation in GTEDGE, the "x-transport pumping" process was utilized to model the x-transport directly into the thermal ion orbit loss fraction, allowing the continuity equation to remain unchanged, but utilizing different F_{therm}^{IOL} curves. Assuming particles can only be transported to the next flux surface, the cumulative particle fraction shifts radially outwards by the integral over the different minimum loss energies between the two processes of IOL and x-transport.

$$\Delta F_n^x = \frac{\int_{W_{min}^x}^{E_{min}^{IOL}} V_0^2 \, f(V_0) \, dV_0}{\int_0^{\infty} V_0^2 \, f(V_0) \, dV_0} = \frac{\left|\Gamma\left(\frac{3}{2}, W_{min}^x\right) - \Gamma\left(\frac{3}{2}, E_{min}^{IOL}\right)\right|}{\Gamma\left(\frac{3}{2}\right)} \tag{46}$$

However, for both x-transport model analyses, only two directions were taken into account, $\xi_0 = \pm 0.5$. To expand the calculations for all directions would require a significant computational effort to include in GTEDGE.

Results from comparing the two models were used to develop assumptions for a simplified implementation into the fluid equations. It is assumed that all x-transported particles will cascade down to the flux surface where ion orbit loss becomes the dominant process, so there is a large source of relatively lower energy, counter-current particles that become newly available to be ion orbit lost. However, the majority of these ions will be immediately lost when this condition is met because low energy, counter-current particles are preferentially lost in the IOL process. Therefore, it is assumed that all of the "x-transport pumped" particles are lost to the plasma just like in conventional ion orbit loss, but this happens on a flux surface closer to the separatrix (ρ=0.943 in this case) than where they were originally displaced. Because these x-transported ions are actually lost via the IOL mechanism, they can be removed from the plasma by modifying the total loss fraction profile, instead of the particle source and sink terms in the continuity equation.

$$F_{loss}^{tot} = \frac{F_{therm}^{IOL} + \sum_{n=1}^{K} \Delta F_n^x}{1 + N_{tot}^x / N_{tot}^{IOL}} \tag{47}$$

K is the flux surface where ion orbit loss becomes dominant, and the sum accounts for the total loss fraction, F_{loss}^{tot}, to be treated as a cumulative profile. The denominator accounts for the presence of more particles on each outer flux surface than originally due to the x-transport, constraining the ratio of x-transported particles, N_{tot}^x, to total number of particles modifies this cumulative fraction to a maximum value of 1.

The x-transport modified cumulative loss profile compared to the conventional thermal ion orbit loss profile is shown in Fig. (29) for the DIII-D H-mode shot #123302.

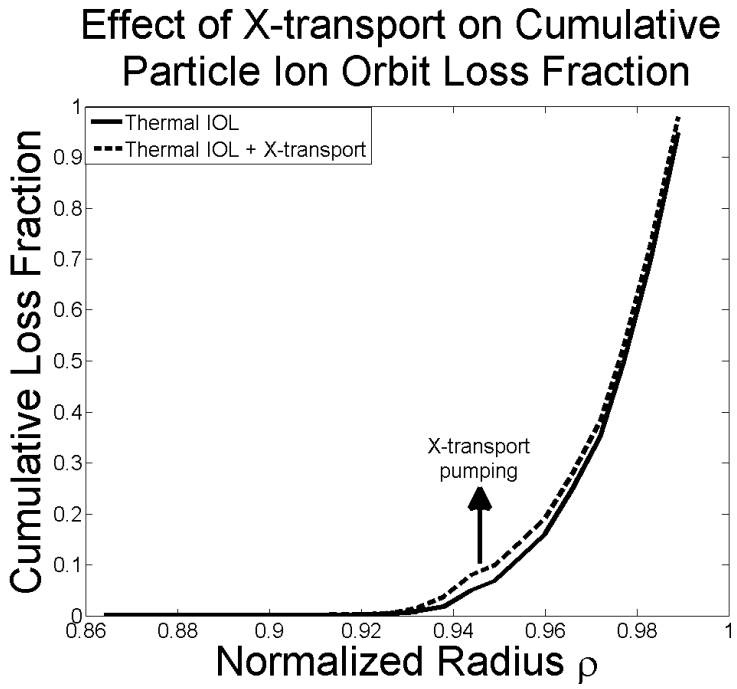

Figure 29: X-transport corrected particle loss fractions.

This restructuring of the cumulative loss fraction curves due to the competing processes of IOL and x-transport increases the particle loss fraction through the steep gradient region of the pedestal as expected. The effect would be amplified with the

inclusion of all pitch angles (not just $\xi_0 = \pm 0.5$) in the analysis, and this will be considered in future work.

CHAPTER 9

PREDICTIVE RADIAL ELECTRIC FIELD AND SENSITIVITY TO ION ORBIT LOSS MODEL IMPROVEMENTS

Ion orbit loss model improvements can be propagated through the fluid equations to calculate the 1) radial particle flux 2) toroidal and poloidal velocities and 3) radial electric field using the overall methodology outlined in Fig. (2). The term "model improvements" refers to the three extensions to ion orbit loss theory previously discussed, which are 1) the inclusion of fast ion orbit loss, 2) the use of experimental flux surfaces and magnetic fields instead of a modified circular geometric model, and 3) the reduction of the amount of ion orbit loss calculated by 40% due to some ions returning into the plasma after executing orbits that cross the separatrix.

The radial particle flux calculated from Eq. (9) and shown in Fig. (30) compares the results with and without improvements to the IOL model as well as to the calculation with no ion orbit loss.

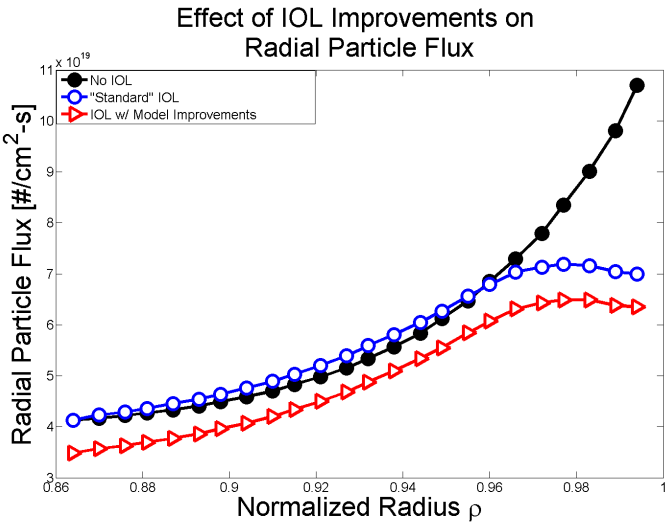

Figure 30: Radial particle flux with and without ion orbit loss model improvements compared to the case without ion orbit loss.

Relative to the calculation without the model improvements, inclusion of fast ion losses appears to dominate by further reducing the radial particle flux profile due to a decrease in ion source. Equations (33) and (35) describe how a change in radial particle flux will drive a change in rotation.

Model improvements to the IOL calculation affect the intrinsic rotation calculation of Eq. (7) as shown in Fig. (31). The use of experimental flux surfaces and magnetic fields appear to dominate the ion orbit momentum loss calculation, causing the prediction of the intrinsic rotation peak to be larger and located closer to the separatrix relative to the prediction of a circular model, which exemplifies the results from the effects of experimental geometry on the cumulative momentum loss fraction. This result concurs with available intrinsic rotation probe measurements [36,86] and CER measurements [39,87] that show peaking at locations at or near the separatrix. (It should be noted that there is uncertainty in the determination of the separatrix location.)

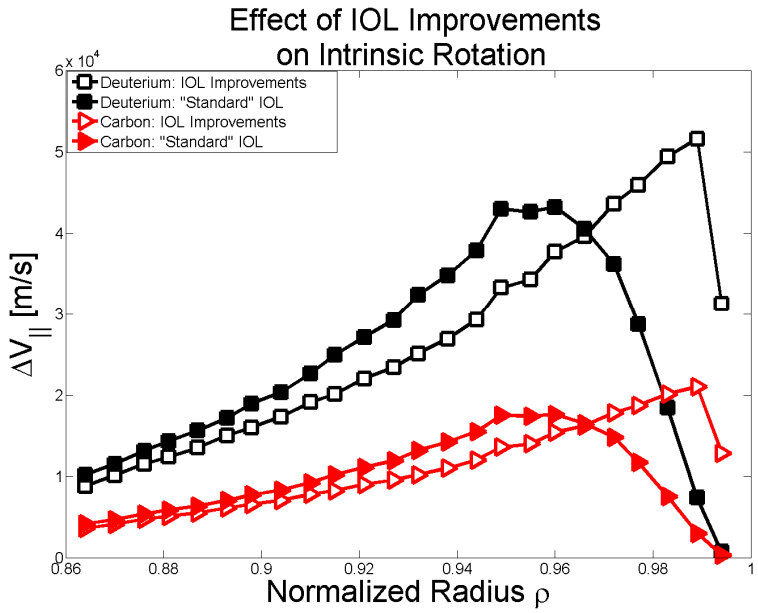

Figure 31: Effect of ion orbit loss model improvements on intrinsic rotation for both deuterium and carbon.

Intrinsic rotation profiles have a profound effect on the poloidal rotation profiles. The total poloidal velocity profiles with and without IOL model improvements are shown in Fig. (32) for both carbon and deuterium. The "experimental" deuterium velocity is determined from the radial deuterium momentum balance equation.

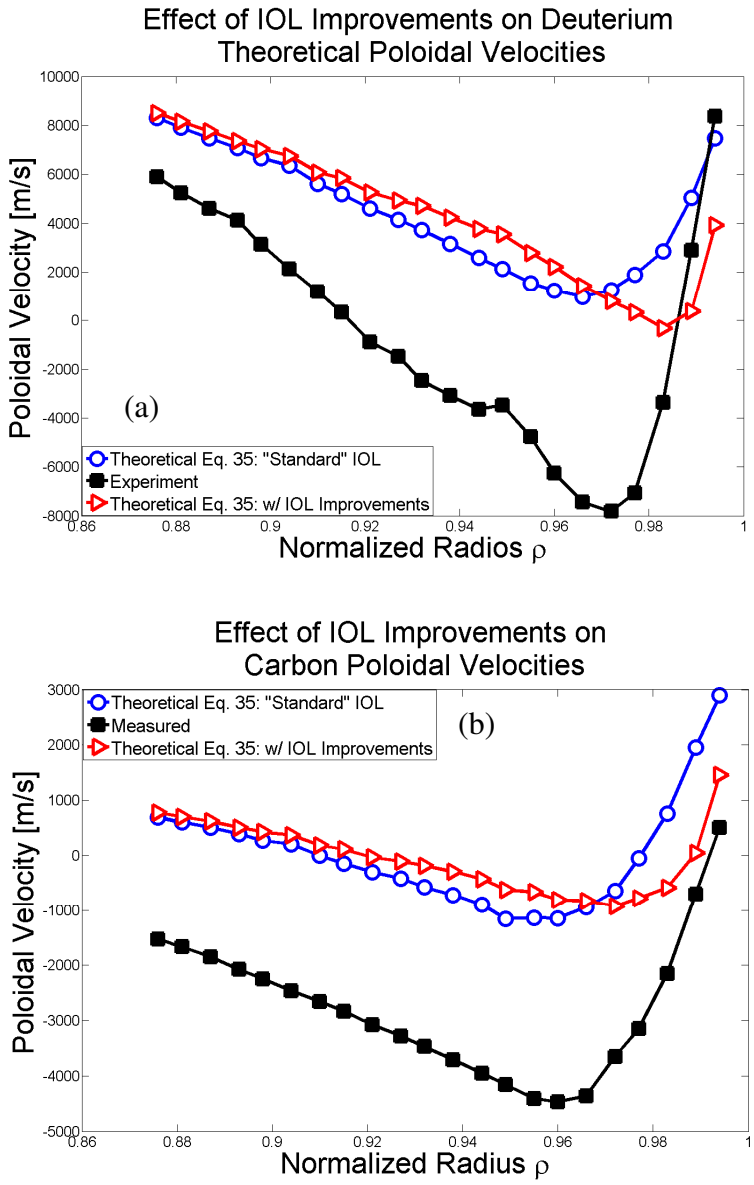

Figure 32: Comparison of theoretical poloidal velocity models with and without ion orbit loss model improvements for a) deuterium and b) carbon.

Predictive poloidal velocity models agree only qualitatively with experimental curves, with the improved IOL model yielding a sharper "well" to the profile that is shifted closer to the separatrix.

The predictive toroidal velocity results with IOL but without momentum loss (IOL1) corrections in Fig. (33) show excellent agreement with experiment, as they should since the momentum transport frequencies ($\nu_{d,j/k}$) were fit to do so. Varied results in the toroidal velocity model with the inclusion of the *ad hoc* intrinsic rotation correction suggest the requirement for the more rigorous implementation of ion orbit loss into the momentum balance equations as discussed in the previous section. The agreement of the general neoclassical fluid model without superposition of intrinsic rotation suggest that the inference of the drag frequencies with the intrinsic rotation correction may be sufficient to account for IOL, but a comprehensive rotational model will be required to prove this preliminary result.

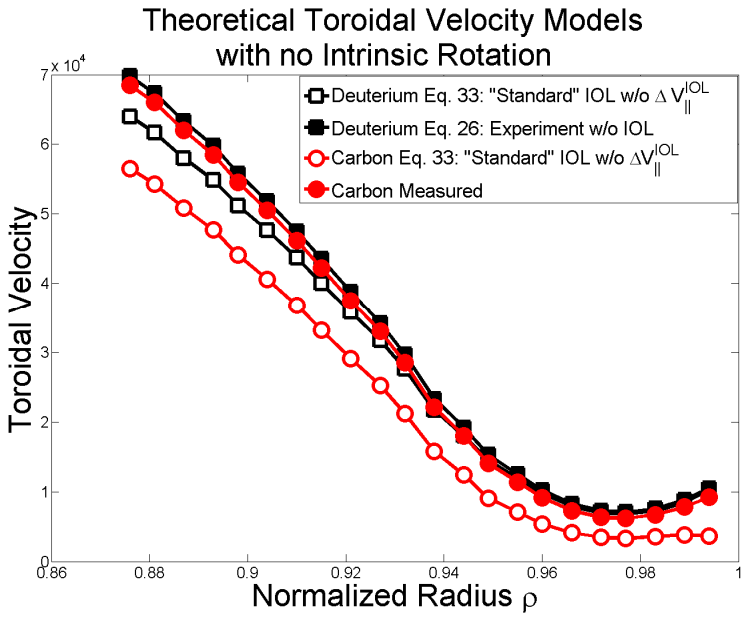

Figure 33: Comparison of theoretical toroidal velocity model with IOL but without intrinsic rotation for both deuterium and carbon. (DIII-D H-mode discharge #123302).

The sensitivity of the radial electric field due to IOL model improvements is seen in Fig. (34). This calculation employs the methodology outlined in Fig. (2) and the toroidal velocity profiles from Fig. (33), which do not have the explicit intrinsic rotation correction but do include the intrinsic rotation in the drag frequency calculation.

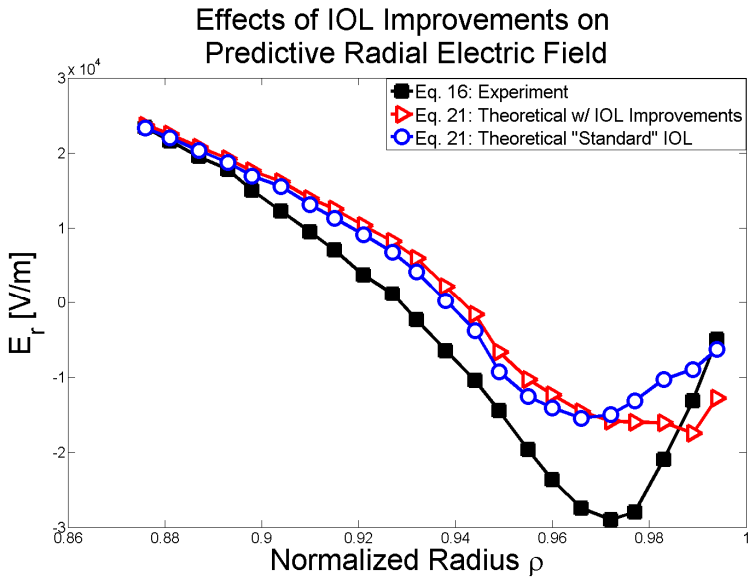

Figure 34: Theoretical radial electric field with and without ion orbit loss model improvements compared to experiment. Theoretical toroidal velocity from Fig. (33) is used in the modified Ohm's Law. (DIII-D H-mode discharge #123302).

With the IOL model improvements, the radial electric field "well" is shifted downwards and outwards. While the predictive E_r "well" still does not align directly with experiment, this is an excellent estimate given the limitations of the fluid model employed.

In order to analyze where the model breaks down, the theoretical model is decomposed into the separate velocity and pressure components to compare with experiment in Fig. (35). It is seen that the differences in primarily the theoretical poloidal

velocity but also the toroidal velocity profiles from experiment contribute to the difference in structure of the radial electric field "well". Similar results are found with the RMP and L-mode discharges, the rotation profiles cause the radial electric field well to be under-predicted (or offset in the L-mode case) using the theoretical model when compared to experiment.

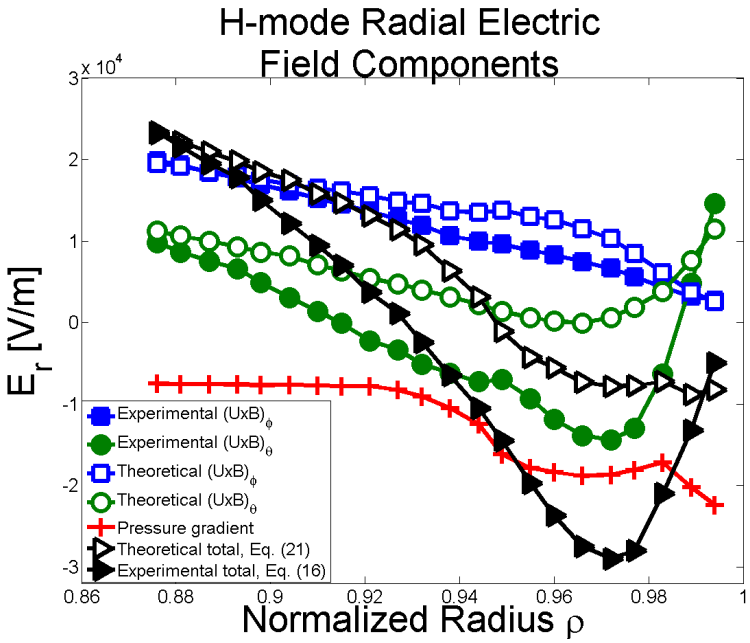

Figure 35: Comparison of the theoretical radial electric field components of toroidal velocity, poloidal velocity, and pressure gradient to experimental components.

CHAPTER 10

GTEDGE COMPARISON TO XGC0

Collaborative research with the Princeton Plasma Physics Laboratory (PPPL) was performed with the primary objective to compare predictions and assumptions of the rapid semi-analytical plasma edge pedestal physics model presented in this dissertation to the state-of-the-art, full-f (but computationally expensive) calculations made by the XGC0 code. Previous simulations using XGC0 interpretively have shown good agreement of measured edge pedestal profiles with DIII-D H-mode discharges [44], especially when including kinetic effects like ion orbit loss to calculate a self-consistent radial electric field. Non-measured quantities such as ion distribution functions and deuterium rotation velocities are also calculated by XGC0, and are of great interest to compare to GTEDGE calculations to inform improvements for future studies.

10.1 XGC0 Methodology

The kinetic neoclassical transport code XGC0 [43] was used to complete goals of the 2011 Fusion Energy Sciences Joint Research Target for understanding the physics mechanisms responsible for the edge pedestal structure with validation of predictive models against experimental data from Alcator C-Mod at MIT, DIII-D at General Atomics, and NSTX at PPPL. XGC0 is a five dimensional (3D in space and 2D in time) code that solves the Hamiltonian guiding center equations developed by Littlejohn, Boozer, and White [88-90], and is designed for use with massively parallel processing systems. The code tracks millions of test particles that undergo Monte Carlo collisions with a background Maxwellian plasma and neutral fluid. This calculation is full-f in that the distribution function of the background plasma is allowed to evolve (or is updated between various stages of the calculation), which will change the calculated energy,

momentum, and position of the test particles after collisions with respect to a calculation where the background plasma is required to be Maxwellian in nature.

Several model parameters, such as the anomalous diffusion coefficient profile, are adjusted as inputs and affect the outcome of the simulated profiles. XGC0 calculates quantities through typical neoclassical transport models [43], and then adjusts the transport profile based on what the user specifies to be anomalous transport. The purpose of adjusting the model parameters is to match certain profiles to experiment. In this case, the electron density, electron temperature, impurity density, impurity temperature, toroidal and poloidal carbon velocities, and the radial electric field are matched to the CER and Thomson scattering system measurements from DIII-D.

Synthetic diagnostics to obtain specific 2-dimensional information about the main ions, carbon impurities, and electrons were constructed by D.J. Battaglia. The outputs from these diagnostics collect information about the three plasma particle populations for 1) parallel energy 2) perpendicular energy 3) weighting distribution function 4) toroidal momentum 5) poloidal momentum 6) radial momentum 7) parallel momentum and 8) particles/dt within each cell at each time at various points between XGC0 modules. Similar to the GTEDGE analysis (and other profile fitting routines in general), XGC0 analyzes a specific time slice for a given shot. In this case, DIII-D QH-mode shot #106999 at 3700ms was selected for analysis. The profiles that are simulated by XGC0 are then compared to the measured CER profiles for this shot and timeslice to determine if agreement between all quantities is possible. One of the major implications of XGC0 H-mode studies in the past few years [44] has been to yield simulated profiles that can be

matched to experiment for all quantities (i.e. a correct radial electric field profile structure corresponds to the predicted pedestal height and width seen in measurements).

The flux-driven guiding center XGC0 code computes the self-consistent electron, ion, and neutral transport for both open and closed field line regions in an axi-symmetric diverted magnetic geometry, including the consideration of recycling of neutrals from the wall. The simulation is divided into 60 radial zones whose thickness correspond to roughly 1mm in DIII-D. The calculation is represented in terms of toroidal transit time, τ, which represents the time it takes for a 200eV passing ion whose velocity vector is parallel to the magnetic field vector along the magnetic axis of a tokamak of major radius R=1m to travel once around the torus. A sufficiently relaxed solution in steady state with appropriate resolution in four dimensions (2D in space, 2D in time) typically requires greater than 50τ time steps and several days of parallel calculations on thousands of processors. This equates to at least one month to turn around a solution when including queue times on large clusters.

For substantiation of the GTEDGE calculations and aid in improving the model presented in this dissertation, a DIII-D QH-mode (non-ELMing) discharge #106999 was simulated with both XGC0 and GTEDGE. The DIII-D QH-mode discharge selected exhibits steady state conditions and high temperatures, leading to increased kinetic effects from the loss of high energy particles, which are desirable for meaningful comparisons between XGC0 and GTEDGE calculations.

To interpret the DIII-D QH-mode discharge with XGC0, profiles for ion diffusion, and ion and electron heat diffusivities were estimated to be of hyberbolic tangent form, as seen in Fig. (36).

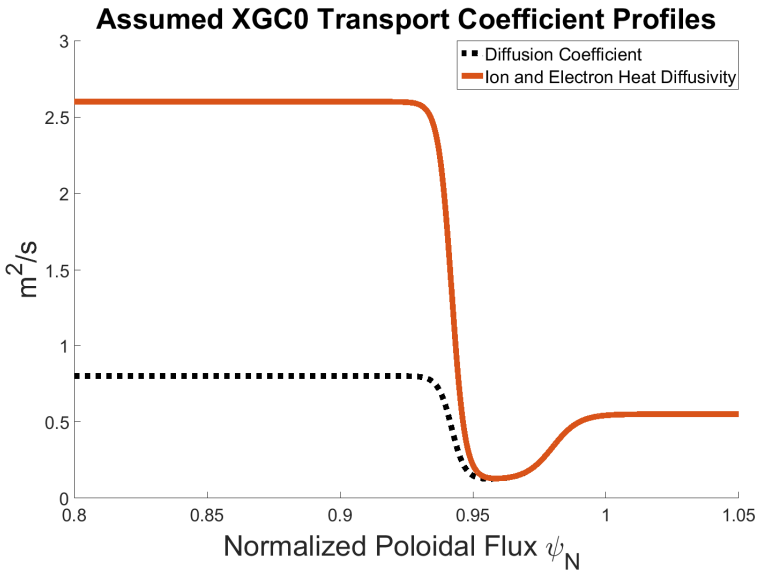

Figure 36: Transport coefficient profiles used in the XGC0 simulation of DIII-D QH-mode discharge #106999.

Particle, heat, and momentum fluxes from the core plasma to the edge plasma were applied as a core boundary condition, and other model parameters such as neutral recycling coefficients were adjusted to the values shown in Table 3 in order to match simulated profiles of electron and ion temperatures and densities to measured experimental profiles.

Table 3: Assumed inputs for XGC0 simulation of DIII-D QH-mode shot #106999.

Simulation Limits, ψ	Neutral Recycling Fraction	Ion Heating Power	Electron Heating Power	Particle Source	Torque Input
[0.8,1.05]	0.95	9.5 MW	1.0 MW	9.0E20 [#/s]	4.0 Nm

With properly adjusted inputs, XGC0 accurately simulates the experimentally measured profiles, as seen in Fig. (37), in conjunction with interpreted (non-measured) quantities like ion distribution functions, deuterium velocities, and radial particle fluxes,

which can readily be compared to similarly calculated GTEDGE quantities.

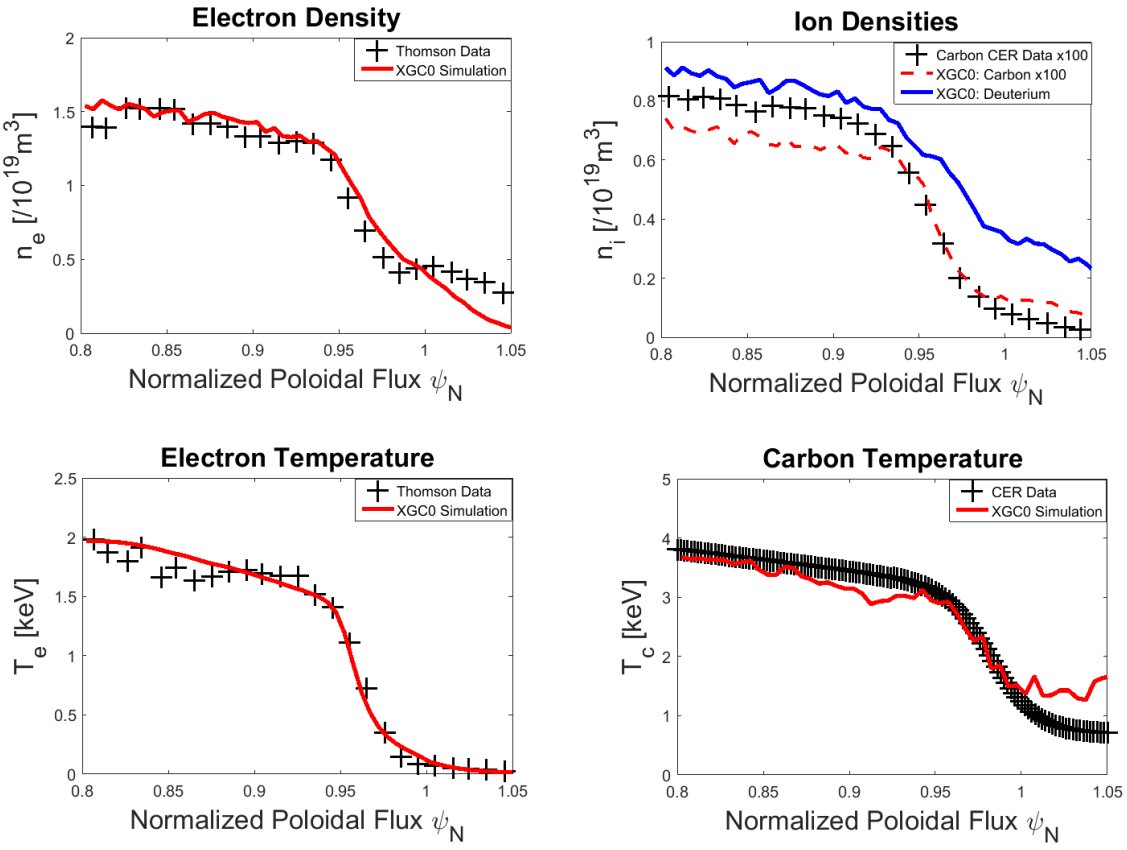

Figure 37: Simulated XGC0 temperatures and densities compared to experiment.

10.2 Comparison of GTEDGE and XGC0 Simulations

With XGC0 simulations predicting correct profiles when compared to the available measured quantities, it is assumed that the non-measured quantities calculated by the code can lend some insight to the GTEDGE model, specifically with regard to the ion orbit loss calculation, radial particle fluxes, rotation velocities, and radial electric field components.

Minimum energy curves constructed from solving Eq. (4) in GTEDGE are compared to the velocity distribution functions simulated from XGC0. The two

dimensional velocity distribution function in parallel versus perpendicular velocity space for deuterium at approximately ρ=0.97 at the outboard midplane is shown in Fig. (38).

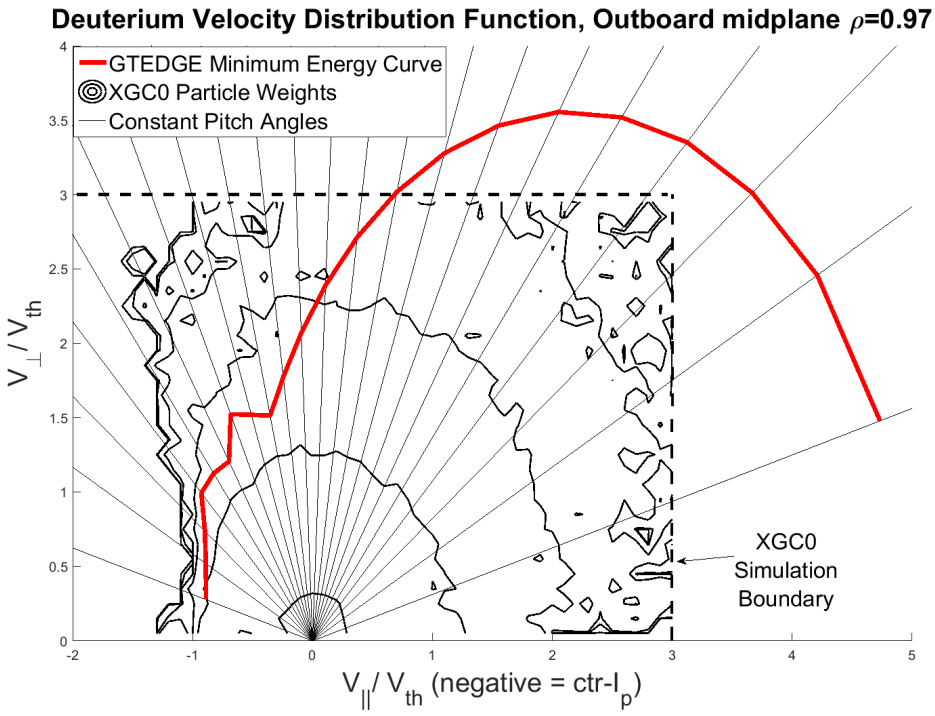

Figure 38: Deuterium velocity distribution simulated from XGC0 compared to calculated minimum energy curves for ion orbit loss from GTEDGE.

The "particle weights" shown by the XGC0 calculation represent the level contours of the particle distribution function $f(\rho, \theta, V_\perp, V_\parallel)$ at a specific radial and poloidal location. A typical Maxwellian curve would be represented by a symmetric arc centered around zero. The GTEDGE minimum energy curve, $E_{min}(\rho, \theta_0, \theta_D, \xi_0)$ represents the boundary above which ion orbit loss causes particles to be removed from the assumed Maxwellian distribution function. In this case, the radial and poloidal angle variables are fixed, and the minimum energy is expressed in terms of a minimum speed as a function of pitch angle.

The deuterium velocity distribution calculated from XGC0 is seen to be asymmetric around $V_{\parallel} = 0$, presumably due to ion orbit loss primarily of counter-current ions, $V_{\parallel} < 0$. The region above the minimum energy curve represents the part of a Maxwellian distribution function that would be removed by the truncated Maxwellian representation of the GTEDGE model, or the lower limit of the integral in Eq. (5). The GTEDGE model for the particle distribution function is seen to align quite well with the simulated distribution function from XGC0, especially for highly counter-current particles. There is some over-prediction of ion orbit loss in the upper left quadrant represented by counter-current ions with $(V_{\parallel}/\,V_{th}, V_{\perp}/\,V_{th}) \sim (-1, 2.5)$ remaining above the predicted minimum energy loss curve from GTEDGE. This can be explained, at least in part, by the inclusion in the XGC0 calculation of ions in the process of being ion-orbit lost, as well as including particles that return to the plasma from the scrape off layer. The radially emanating lines represent constant pitch angle, and the minimum energy curve calculated from GTEDGE terminates at $\xi_0 = \pm 0.99$.

If the XGC0 distribution function, $f(\rho, \theta, V_{\perp}, V_{\parallel})$, is integrated over the perpendicular velocity, a 1-dimensional (in velocity) distribution function can be computed, $f(\rho, \theta, V_{\parallel})$. The loss hole describing the difference between the deuterium ion velocity 1D distribution function including ion orbit loss compared to a symmetric distribution function assumed to not include ion orbit loss is shown in Fig. (39) by the shaded regions. Since the GTEDGE distribution function is not a function of the pitch angle, but instead is integrated with limits that are functions of the pitch angle, a similar curve cannot be computed for comparison in this case.

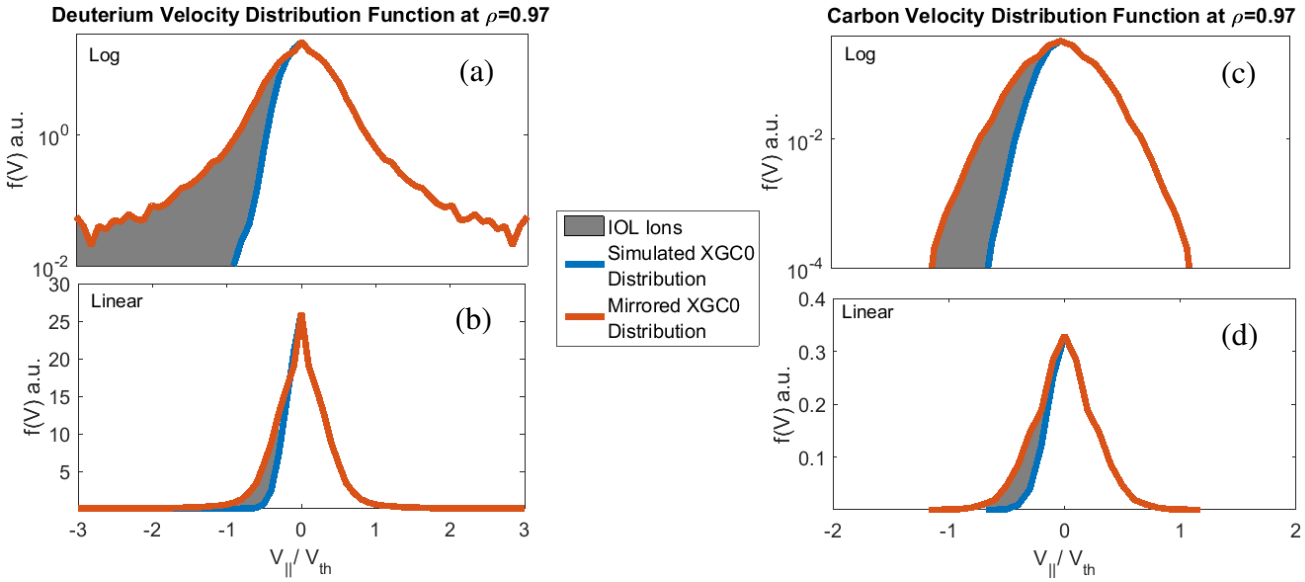

Figure 39: Simulated one dimensional distribution function from XGC0 showing skewed profiles for deuterium species shown in (a) and (b), but not as significantly for carbon shown in (c) and (d).

Figure (39) shows the simulated deuterium velocity distribution function as highly skewed towards high energy co-current ions, with a loss of IOL particles in the shaded counter current regions. The carbon impurity distribution functions are seen to be simulated as much closer to Maxwellian in nature, with only a slight asymmetry attributable to ion orbit loss.

Assuming the asymmetry in the ion distribution functions is solely due to ion orbit loss, the difference between the simulated XGC0 distribution function and a symmetric distribution with no IOL will yield the fraction of lost particles. By integrating the shaded region of the XGC0 1D distribution function and dividing by the integral over the full distribution function, a loss fraction profile can be constructed. This cumulative integral for the XGC0 simulated distribution function can be directly compared to the

truncated Maxwellian integral used by GTEDGE, which describes the cumulative particle loss fractions for the plasma as a function of normalized radius.

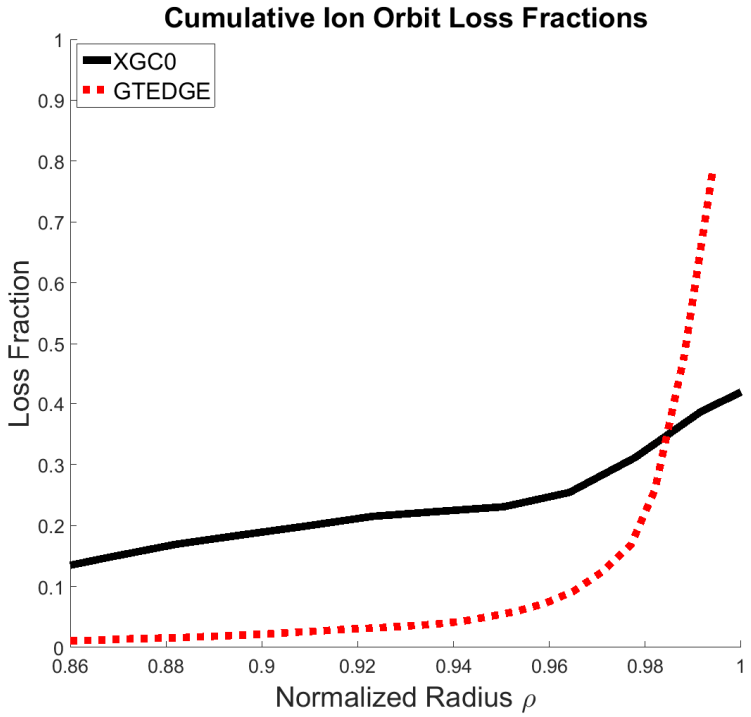

Figure 40: Edge pedestal cumulative loss fractions calculated from XGC0 and GTEDGE.

The total cumulative loss fractions calculated from XGC0 are seen to be less than GTEDGE, which is consistent with the velocity distribution function visualization in Fig. (38), but predict more ion losses throughout the entire profile in the edge region. This result is consistent with the decreased total IOL predicted by using experimental flux surfaces (relative to the circular approximation) and magnetic fields in section 6.2, and the increase in loss fraction in the inner pedestal region through the x-transport pumping mechanism described in chapter 8.

The GTEDE model uses the ion orbit loss fractions as a loss term in the fluid continuity equation determining the radial particle flux of the thermalized ions. The

GTEDGE calculation is based on a radial particle flux boundary condition at ρ=0.86, which includes all thermalized ion sources for $r' \leq 0.86$, $\Gamma(\rho = 0.86) = \int_0^{0.86} \frac{r'}{0.86} [n(r')v_{ion}(r') + \hat{S}_{nbi}(r')]dr'$. The XGC0 radial particle flux is determined by the difference in radial currents calculated between cells for each particle for collisional diffusion processes as well as collisionless neoclassical transport. The two particle fluxes are compared in Fig. (41).

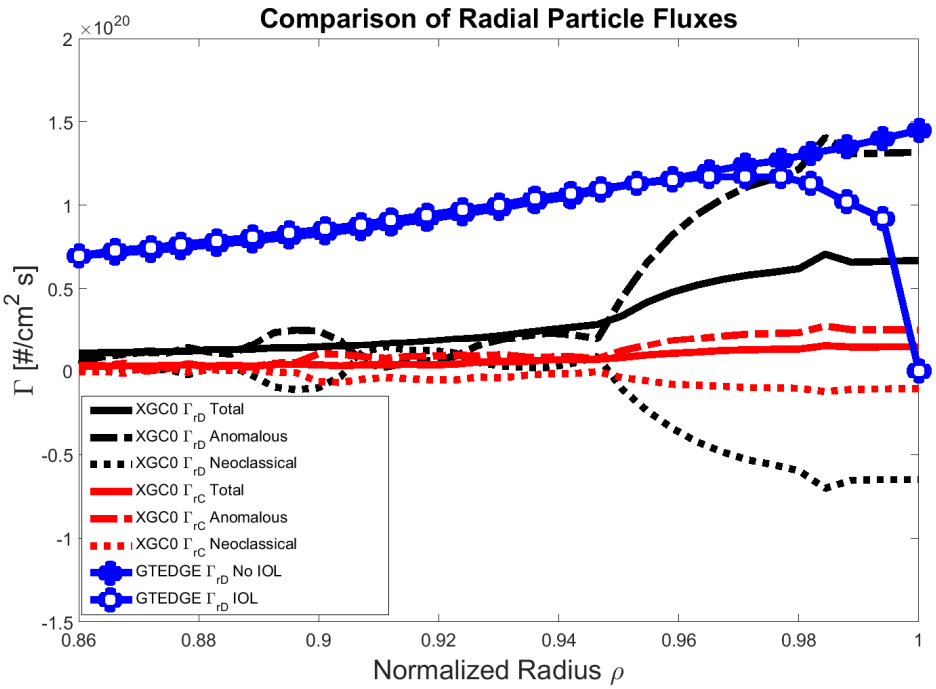

Figure 41: Comparison of radial particle fluxes for both carbon and deuterium calculated from GTEDGE and XGC0.

The disparity in fluxes from GTEDGE and XGC0 could be due to different return currents associated with ions in the XGC0 calculation than those that are included in the GTEDGE calculation, a specific assumption in the neutral recycling model, or the different methodologies used in calculating the radial particle fluxes (kinetic versus fluid), but this is not yet fully understood. The carbon radial particle flux simulated by

XGC0 is roughly 20% as large as the main ion radial particle flux, suggesting that the assumption of a negligible carbon flux in GTEDGE is a reasonable initial assumption. Neither XGC0 nor the GTEDGE model include different charge states of carbon, which is a reasonable assumption for high energy and low collisionality edge pedestal regions like this particular QH-mode; however, will need to be considered for more accurate treatment of varied modes of operation.

One distinction between XGC0 and GTEDGE is the ability for XGC0 to simulate local velocities, whereas GTEDGE calculates flux surface averaged (FSA) velocity profiles. The toroidal velocities calculated from XGC0 are constructed from a tally of the toroidal momentum for each particle species in each cell, normalized by the mass and weighting function for each species and location. Toroidal velocities calculated by the two codes are compared in Fig. (42), including both the outboard midplane (OBM) and FSA profiles for both carbon and deuterium. The GTEDGE predicted velocities are calculated from Eq. (33).

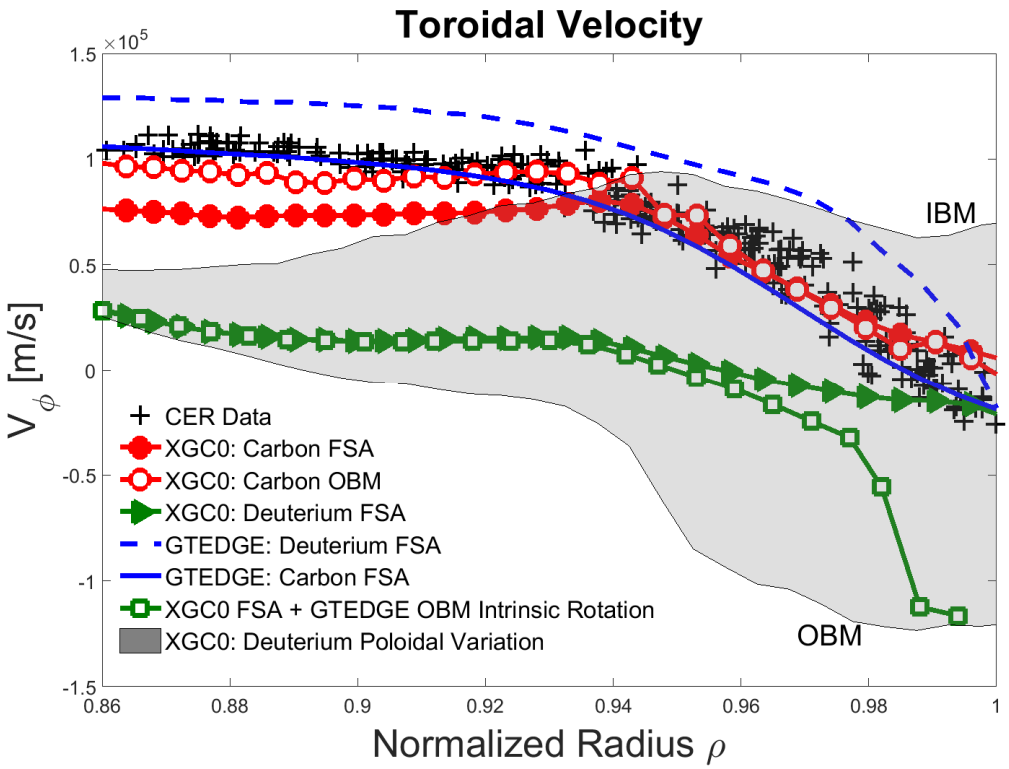

Figure 42: Carbon and deuterium toroidal velocities from XGC0 (FSA and OBM) compared to GTEDGE (FSA) and the CER experimental measurement for carbon.

When comparing the GTEDGE calculation with the CER experimental measurements, it is seen that the predictive carbon FSA toroidal velocities match extremely well with experiment. The predictive toroidal velocity formalism is determined from the theory presented in section 5.1 which calculates rotation for thermalized ions that are not ion orbit lost using a viscosity coefficient that was chosen to match experiment. The deuterium toroidal velocity calculation predicts larger rotation for the main ion than the impurity species, but with a similar structure profile.

XGC0 inputs were adjusted to match experimental OBM carbon data, therefore the OBM carbon velocities align very well with measurements from the CER system. The flux surface average carbon profiles take on a slightly different structure than those

measured at the outboard midplane, but are still very similar to the OBM profiles. The XGC0 simulated FSA deuterium rotation profiles are starkly different than experimental carbon measurements, with roughly a four times reduction in magnitude as well as a change in sign in the profile around the transport barrier at roughly $\rho \sim 0.98$. The XGC0 simulated deuterium OBM velocity is drastically different than the flux surface average and even exhibits a sign reversal for the majority of the profile. There may be inherent assumptions in XGC0 regarding how the torque input is divided between carbon and deuterium species, and in the low collisionality regime of this shot, there is not much momentum transfer between species.

The predicted FSA carbon rotation profiles agree well between XGC0 and GTEDGE as well as with experimental data. The deuterium velocity profiles differ significantly in both structure and magnitude. An interesting observation from reference [50] is that the majority of ion orbit loss is calculated to cross the separatrix at the outboard midplane, and can sometimes even be larger than the calculated fluid velocity. Assuming the XGC0 deuterium rotation profiles are reliable for this argument, the result from [50] in conjunction with the OBM profiles shown in Fig. (42) and the significantly larger IOL predicted for deuterium than for carbon, suggest that the concentration of ion orbit loss at the outboard midplane could be the cause of the considerably different OBM rotation profiles for deuterium.

The shaded region in Fig. (42) shows the region spanned by the XGC0 deuterium toroidal velocity profiles as they vary poloidally along the flux surface. The OBM toroidal velocity profiles are preferentially in the counter-current direction, and the inboard midplane (IBM) profiles are largely in the co-current direction. This result is

consistent with the XGC0 simulation containing a significant number of IOL particles in the OBM, which would be preferentially in the counter-current direction. The FSA minus the localized OBM intrinsic rotation in Fig. (42) shows order of magnitude agreement with the difference between the FSA and the OBM toroidal velocity boundary at the far edge near the separatrix, suggesting this could be the mechanism for the significantly different deuterium profiles than those of carbon, which will affect the radial electric field calculation as discussed previously. Taking into account the flatter loss fraction structure predicted in XGC0 in comparison to GTEDGE, the effects of intrinsic rotation may extend much farther into the edge than predicted by GTEDGE if a similar calculation could be performed with XGC0.

The fraction of lost particles as a function of poloidal angle calculated from GTEGE shows that IOL particles are preferentially lost to the OBM in this QH-mode discharge, supporting the above argument for ion orbit loss as the driver for the large poloidal variation between the IBM and OBM deuterium toroidal velocity profiles.

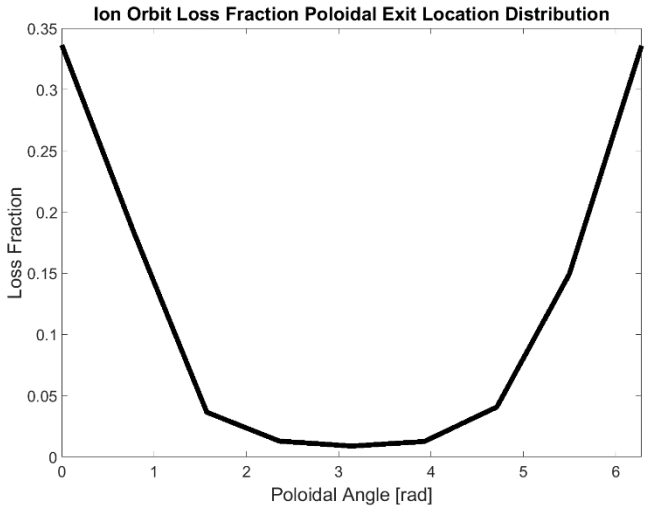

Figure 43: Poloidal distribution of exit location of ion orbit loss particles.

Similar comparisons are made for poloidal velocity profiles in Fig. (44).

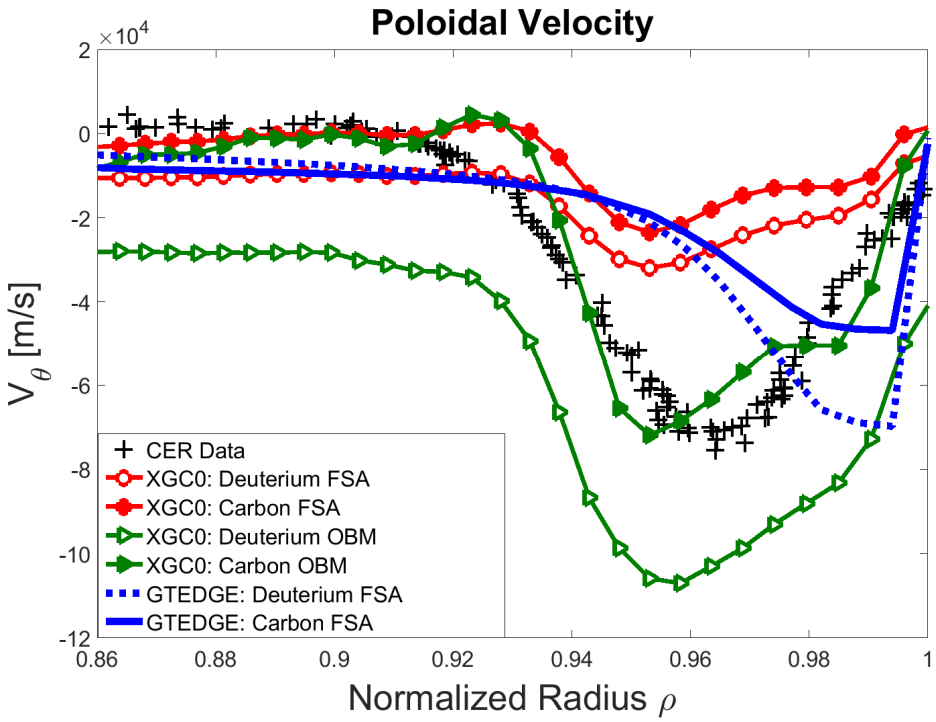

Figure 44: Carbon and deuterium poloidal velocities from XGC0 (FSA and OBM) compared to GTEDGE (FSA) and the CER experimental measurement for carbon.

Flux surface averaged poloidal velocity profiles calculated from GTEDGE predict a smaller "well" for carbon than for deuterium, with both shifted closer to the separatrix with respect to the experimental carbon CER measurements.

The XGC0 outboard midplane carbon poloidal velocity profile predicts the experimental value quite well; however, the FSA poloidal velocity profiles for both carbon and deuterium show a smaller magnitude "well" structure than the OBM CER measurements. The OBM deuterium poloidal velocity profile is larger in magnitude in the negative direction, exemplifying similarities to the E_r profile structure.

Both XGC0 and GTEDGE predict a deeper poloidal velocity "well" for deuterium than for carbon, which provides a greater contribution to the Ohm's Law radial electric field calculation "well" than for the carbon ion. However, the GTEDGE FSA poloidal

velocity profiles calculate "well" depths between the FSA and OBM "wells" simulated from XGC0.

The radial electric field is determined differently in XGC0 than the Ohm's Law expression developed in this dissertation, $E_r^{Ohm} = \eta j_r + u \times B - \nabla p$. In the XGC0 simulation, the electrostatic potential is assumed to be constant along flux surfaces, and the radial electric field is evaluated according to the radial Ampere's law averaged over a flux surface [43].

$$4\pi\langle \boldsymbol{J} \cdot \nabla\psi \rangle + {}^{\partial}/_{\partial t} \langle \boldsymbol{E} \cdot \nabla\psi \rangle = c\langle \nabla \cdot (\boldsymbol{B} \times \nabla\psi) \rangle = 0 \tag{48}$$

The brackets represent the flux surface average and **J** is the sum of all the current in the plasma, including the classical polarization currents included in Poisson's equation. This calculation is not valid in the open field line region for XGC0, and is appropriately compared to the GTEDGE radial electric field inside the separatrix in Fig. (45).

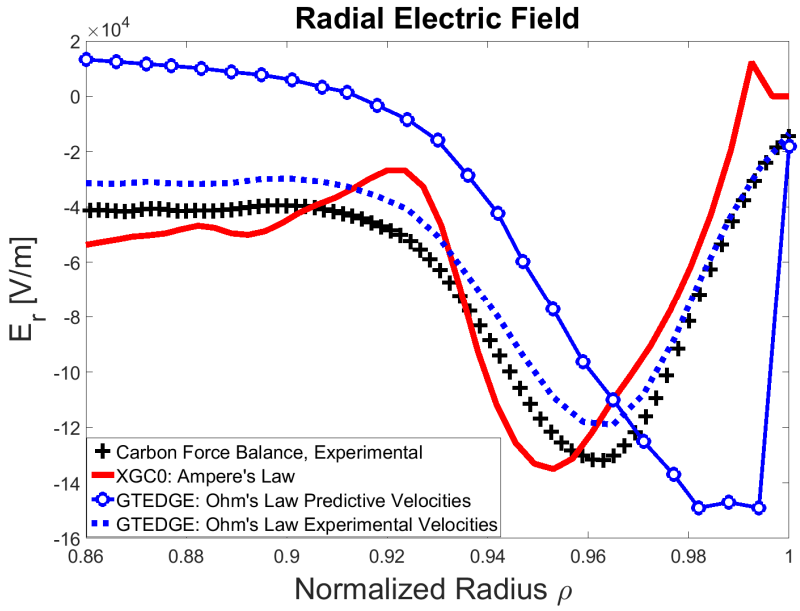

Figure 45: Comparison of radial electric field profiles calculated from XGC0, GTEDGE, and the carbon radial momentum balance equation.

All radial electric field profiles predict similar structure and "well" depth relative to experiment (carbon force balance). The GTEDGE "well" using predictive velocities is closer to the separatrix than the XGC0 and experimental profiles, which can be seen to arise from the predictive poloidal velocity profiles in Fig. (44). As previously discussed, the GTEDGE prediction of the radial electric field using experimental rotation profiles is in good agreement with experiment. The XGC0 simulation is within the same error (~20%) to experiment as the GTEDGE Ohm's Law calculation using experimental velocities, illustrating that if better velocity models can be constructed, the proposed Ohm's Law calculation can be just as an effective tool for calculating the radial electric field, but with significantly less computational effort.

CHAPTER 11

DISCUSSION AND CONCLUSIONS

A modified Ohm's Law is presented with the goal of developing a computationally efficient predictive model for the calculation of the radial electric field in the plasma edge. The Ohm's Law formalism is based on a multi-fluid momentum balance model that employs a Lorentz friction model for two plasma species. The Ohm's Law E_r prediction is validated by demonstrating its consistency with the usual carbon radial momentum balance evaluation of E_r in three DIII-D discharges of representative H-mode, RMP, and L-mode plasmas when experimental rotation profiles are used to evaluate the motional electric field. The Ohm's Law E_r calculation is rapid, and can readily be extended to a first principles predictive calculation by using predictive edge velocity models which include effects of ion orbit loss, intrinsic rotation, and return currents.

In order to leverage the modified Ohm's Law as a predictive calculation, a semi-analytical model for the edge plasma is developed to quantitatively describe the relationship between edge parameters that determine the radial electric field. Ion orbit loss and corresponding return currents generate a radial particle flux and intrinsic rotation in both the toroidal and poloidal directions. The radial particle flux and intrinsic rotation torque the plasma and determine the plasma rotation profiles. The plasma rotation then generates a motional radial electric field, which affects the amount of ion orbit loss. Previous ion orbit loss models are extended to account for fast neutral beam ion losses, realistic geometrical representations for flux surfaces and magnetic fields, the effects of ions returning from the scrape off layer, and the x-transport of ions in the low-B region near the x-point.

Relative to the previous ion orbit loss model, inclusion of prompt fast neutral beam ion orbit lost particles decreases the radial particle flux profile due to a reduced source term in the continuity equation. Using realistic magnetic fields and flux surface geometry in the ion orbit loss model decreases the total amount of particle and energy losses relative to predictions using simpler magnetic field representations, while increasing the amount of momentum loss and shifting the intrinsic rotation peak closer to the separatrix, in better agreement with experimental observations.

A numerical study of orbit tracking predicts that roughly half of the particles that satisfy the momentum and energy balance requirements to be ion orbit lost across the separatrix will directly strike the wall. The other half may re-enter the plasma or may be removed from the plasma via a secondary mechanism such as charge exchange in the scrape off layer.

In-depth particle tracking in the x-region to analyze x-transport reveals a new mechanism, “x-transport pumping”, which transports (via grad-B and curvature drifts) lower energy ions on internal flux surfaces to outer flux surfaces where they are energetically able to be ion orbit lost. This effect can be included in the cumulative thermal ion orbit loss fraction for incorporation into the fluid equations, but future research is required for actual implementation into the GTEDGE fluid equations.

Momentum balance rotation models for toroidal and poloidal velocities (which depend on ion orbit loss and intrinsic rotation) are leveraged for calculating the motional component of the radial electric field in the predictive E_r calculation. When the improved ion orbit loss model is used in the completely predictive edge pedestal model, the predicted poloidal rotation profile agrees in order of magnitude and general profile with

experiment, and the effects of intrinsic rotation improve the agreement. The theoretical toroidal velocity profile with particle IOL corrections (but without the explicit inclusion of intrinsic rotation) predicts profiles in very good agreement with experiment. When the experimental velocity profiles were used in the modified Ohm's Law, the theoretical radial electric field calculation predicts a profile quite close to experiment. The improvements introduced in this work to the ion orbit loss calculation act to decrease the radial electric field "well" slightly and shift it towards the separatrix.

To compare the proposed methodology with another approach, results from DIII-D QH-mode shot #106999 calculated by GTEDGE were compared to an XGC0 simulation. Comparisons of ion orbit loss cones reveal that the truncated Maxwellian model used in GTEDGE is a good approximation for the non-Maxwellian velocity distribution in the far edge region. XGC0 calculates little carbon ion orbit loss, suggesting the need to include it in future GTEDGE analysis should be further analyzed. Radial particle flux comparisons show very similar profile structures for the kinetic XGC0 and the fluid GTEDGE calculation based on the continuity equation; however, the GTEDGE core boundary condition based on core particle balance is an order of magnitude higher than that of XGC0, and this difference is not yet understood. The assumption of negligible carbon radial particle flux made in GTEDGE is affirmed as reasonable by the small radial carbon flux profiles predicted by XGC0.

Simulated deuterium velocities from XGC0 predict starkly different profiles to those of the carbon impurity due to the low edge collisionality in the QH-mode discharge. Intrinsic rotation due to ion orbit loss at the outboard midplane can be used to explain the poloidal variation of the deuterium velocity profiles. Calculated intrinsic rotation from

GTEDGE give order of magnitude estimates for the difference between the flux surface average deuterium toroidal velocity predicted by XGC0 and that localized to the outboard midplane.

The radial electric field comparisons show that the Ohm's Law calculation in GTEDGE using experimental velocities predicts the radial electric field in similar agreement with experiments as the XGC0 simulation, demonstrating that the GTEDGE radial electric field calculation with IOL has the potential to be just as an effective tool with much less computational expense.

Since the Modified Ohm's Law was seen to predict the radial electric field within 10% of experiment when experimental rotation velocity profiles were used, future work will focus on improving the toroidal and poloidal rotation models. One possible mechanism for improving both velocity models is to account for toroidal non-axisymmetry in the fluid viscosity models [91]. This would change the inherent structure of the viscous stress tensor [69,70], and hence the momentum balance equations, by nonlinearly coupling the poloidal and toroidal components.

An interesting possibility conceived but not developed in this research is the idea of using the preferential loss of counter current ions that drive intrinsic rotation to an advantage. It is projected that ITER will be sufficiently large so that NBI will not provide significant torque to the plasma core to drive rotation, which is stabilizing for the plasma. There is the possibility of driving additional rotation if ion orbit loss cone structures can be accurately modeled with correctly correlated intrinsic rotation from the lost ions. It would be possible to inject neutral beam ions in the counter current direction in the edge pedestal region directly into the loss cone with the intention of driving tailored intrinsic

rotation profiles. This research sets the foundation for the basic physics models that would be needed for this calculation, and could be improved to analyze the possibility of generating greater rotation scenarios for large reactors like ITER.

REFERENCES

[1] United Nations, Department of Economic and Social Affairs, World Population Prospects: 2012 Revision, June 2013. http://esa.un.org/unpd/wpp/index.htm

[2] Paris Agreement, FCCC/CP/2015/L.9/Rev.1, Paris Climate Change Conference (COP21), Twenty-first Session, November 30 to December 11, 2015, Paris, France.

[3] A. Hubbard, Plasma Phys. Control. Fusion **42**, A15 (2000)

[4] J.E. Kinsey, G. Bateman, T. Onjun, A.H. Kritz, A. Pankin, G.M. Staebler, and R.E. Waltz, Nucl. Fusion **43**, 1845 (2003)

[5] R. Aymar, V.A Chuyanov, M. Huguet, Y. Shimomura, ITER Joint Central Team, and ITER Home Teams, Nucl. Fusion **41**, 1301 (2001)

[6] M. Kotschenreuther, W. Dorland, Q. P. Liu et al., Proceedings of the 16th Conference on Plasma Physics Controlled Fusion Research, Montreal, 1996 (IAEA, Vienna, 1997), Vol. 2, p 371.

[7] J. E. Kinsey, R. E. Waltz, and D. P. Schissel, Proceedings of the 24th European Physical Society, Berchtesgarten, 1997, Vol. III, p 1081

[8] T.H. Osborne, R.J. Groebner, L.L Lao, A.W. Leonard, R. Maingi, R.L. Miller, G.D. Porter, D.M. Thomas, and R.E. Waltz, Plasma Phys. Controlled Fusion **40**, 845 (1998)

[9] W.M. Stacey, R.J. Groebner, and T.E. Evans, Nucl. Fusion **52**, 114020 (2012)

[10] W.M. Stacey, Phys. of Plasmas **18**, 102504 (2011)

[11] K.H. Burrell, Phys. Plasmas **4**, 1499 (1997)

[12] P.W. Terry, Rev. Mod. Phys. **72**, 109 (2000)

[13] K. H. Burrell, T. N. Carlstrom, E. J. Doyle, P. Gohil, R. J. Groebner, T. Lehecka, N. C. Luhmann Jr., H. Matsumoto, T. H. Osborne, W. A. Peebles, and R. Philipona, Phys. Fluids B **2**, 1405 (1990)

[14] K.H. Burrell, T.N. Carlstrom, E.J. Doyle, D. Finkenthal, P. Gohil, R.J. Groebner, D.L. Hillis, J. Kim, H. Matsumoto, R.A. Moyer, T.H. Osborne, C.L. Rettig, W.A. Peebles, T.L. Rhodes, H. StJohn, R.D. Stambaugh, M.R. Wade, and J.G. Watkins, Plasma Phys. Control. Fusion **34**, 1859 (1992)

[15] K. Ida, S. Hidekuma, Y. Miura, T. Fujita, M. Mori, K. Hoshino, N. Suzuki, and T. Yamauchi, Phys. Rev. Lett. **65**, 1364 (1990)

[16] T. E. Evans, R.A. Moyer, P.R. Thomas, J.G. Watkins, T.H. Osborne, J.A. Boedo, E.J. Doyle, M.E. Fenstermacher, K.H. Finken, R.J. Groebner, M. Groth, J.H. Harris, R.J. La Haye, C.J. Lasnier, S. Masuzaki, N. Ohyabu, D.G. Pretty, T.L. Rhodes, H. Reimerdes, D.L. Rudakov, M.J. Schaffer, G. Wang, and L. Zeng, Phys. Rev. Lett. **92**, 235003 (2004)

[17] T.E. Evans, R.A. Moyer, J.G. Watkins, T.H. Osborne, P.R. Thomas, M. Becoulet, J.A. Boedo,E.J. Doyle, M.E. Fenstermacher, K.H. Finken, R.J. Groebner, M. Groth, J.H. Harris, G.L. Jackson, R.J. La Haye, C.J. Lasnier, S. Masuzaki, N. Ohyabu, D.G. Pretty, H. Reimerdes, T.L. Rhodes, D.L. Rudakov, M.J. Schaffer, M.R. Wade, G. Wang, W.P. West and L. Zeng, Nucl. Fusion **45**, 595 (2005)

[18] J.S. deGrassie, R.J. Groebner, and K.H. Burrell, Phys. of Plasmas **13**, 112507 (2006)

[19] V. Rozhansky and M. Tendler, Phys. Fluids B **4**, 1877 (1992)

[20] J.-P. Floyd, W.M. Stacey, R.J. Groebner and S.C. Mellard, Phys. of Plasmas **22**, 022508 (2015)

[21] F.L. Hinton, Y.B. Kim, Nucl. Fusion **34**, 899 (1994)

[22] L.G. Askinazi et al, Nucl. Fusion **32**, 271 (1992)

[23] W.M. Stacey et al, Phys. Plasmas **20**, 012509 (2013)

[24] K Itoh, S-I Itoh, K Kamiya and N Kasuya, Plasma Phys. Control. Fusion **57**, 075008 (2015)

[25] S.P. Hirshman, Nucl. Fusion **18**, 917 (1978)

[26] T.D. Rognlien, G.D. Porter, and D.D. Ryutov, Jour. of Nuclear Materials, **266-269**, 654-659 (1999)

[27] W.M. Stacey, Phys. of Plasmas **9**, 3082 (2002)

[28] W.M. Stacey, Contrib. Plasma Phys. **4-6**, 524-528 (2014)

[29] K. Miyamoto, Nucl. Fusion **36**, 927 (1996)

[30] W.M. Stacey, Phys. Plasmas **5**, 1015 (1998)

[31] W.M. Stacey, Phys. Plasmas **8**, 3673 (2000)

[32] W.M. Stacey, Nucl. Fusion **40**, 965 (2000)

[33] A.V. Chankin and G.M. McCracken, Nucl. Fusion **33**, 1459 (1993)

[34] J.S. deGrassie, Plasma Phys. Control. Fusion **51**, 124047 (2009)

[35] P. Helander, R. J. Akers, and L.-G. Eriksson, Phys. Plasmas **12**, 112503 (2005)

[36] W.M. Stacey, J.A. Boedo, T.E. Evans, B.A. Grierson and R.J. Groebner, Phys. Plasmas **19**, 112503 (2012)

[37] J.S. deGrassie, J.A. Boedo and B.A. Grierson, Phys. Plasmas **22**, 080701 (2015)

[38] T. Stoltzfus-Dueck, A.N. Karpushov, O. Sauter, B.P. Duval, B. Labit, H. Reimerdes, W.A. J. Vijvers, Y. Camenen, and the TCV Team, Phys. Rev. Lett. **114**, 245001 (2015)

[39] W.M. Stacey and B.A. Grierson, Nucl. Fusion **54**, 073021 (2014)

[40] D. J. Battaglia, K.H. Burrell, C.S. Chang, S. Ku, J.S. deGrassie and B.A. Grierson, Phys. Plasmas **21**, 072508 (2014)

[41] J. Seo, C. S. Chang, S. Ku, J. M. Kwon, W. Choe, and Stefan H. Müller, Phys. Plasmas **21**, 092501 (2014)

[42] C.S. Chang, S. Kue, and H. Weitzner, Phys. of Plasmas **9**, 3884 (2002)

[43] C.S. Chang, S. Kue, and H. Weitzner, Phys. Plasmas **11**, 2649 (2004)

[44] D. J. Battaglia, K. H. Burrell, C. S. Chang, S. Ku, J. S. deGrassie and B. A. Grierson, Phys. Plasmas **21**, 072508 (2014)

[45] J.A. Heikkinen and S.K. Sipila, Phys. Plasmas **2**, 2724 (1995)

[46] T.D. Rognlien, J.L. Milovich, M.E. Rensink et al, J. Nucl. Mater., **196-198,** 347 (1992)

[47] D.P. Coster, X. Bonnin, Corrigan et al, J. Nucl. Mater., **337-339**, 366 (2005)

[48] R. Schneider, X. Bonnin, K. Borrass et al, Contrib. Plasma Phys., **46**, 3 (2006)

[49] J.S. deGrassie et al, Nucl. Fusion **49**, 085020 (2009)

[50] W.M. Stacey and M.T. Schumman, Phys. Plasmas **22**, 042504 (2015)

[51] T.M. Wilks and W.M. Stacey, Submitted to Phys. Plasmas

[52] W.M. Stacey and T.M Wilks, Phys. Plasmas **23**, 012508 (2016)

[53] W.M. Stacey, Phys. of Plasmas **18**, 122504 (2011)

[54] F.L. Hinton and R.D. Hazeltine, Rev. Mod. Phys. **48**, I (1976)

[55] Y.B. Kim, P.H. Diamond, and R.J. Groebner, Phys. Fluids B **3**, 2050 (1991)

[56] W.M. Stacey and R.J. Groebner, Phys. Plasmas **16**, 102504 (2009)

[57] P. Gohil, K. H. Burrell, R. J. Groebner, J. Kim, W. C. Martin, E. L. McKee, and R. P. Seraydarian, in Proceedings of the 14th IEEE/NPSS Symposium Fusion Engineering (1991), p. 1199.

[58] B.A. Grierson, K.H. Burrell, C. Chrystal, R.J. Groebner, D.H. Kaplan, W.W. Heidbrink, J.M. Munoz Burgos, N.A. Pablant, W.M. Solomon, and M.A. Van Zeeland, Rev. Sci. Instrum. **83**, 10D529 (2012)

[59] B.A. Grierson, K.H. Burrell, W.W. Heidbrink, M.J. Lanctot, N.A. Pablant, and W.M. Solomon Phys. Plasmas **19**, 056107 (2012)

[60] T. N. Carlstrom, G. L. Campbell, J. C. DeBoo, R. Evanko, J. Evans, C. M. Greenfield, J. Haskovec, C. L. Hsieh, E. McKee, R. T. Snider, R. Stockdale, P. K. Trost and M. P. Thomas Rev, Sci. Instrum. **63**, 4901 (1992)

[61] W.M. Stacey and R.J Groebner, Phys. Plasmas **15**, 012503 (2008)

[62] W.M. Stacey and T.E. Evans, Nucl. Fusion **51**, 013007 (2011)

[63] T.M. Wilks, W.M. Stacey, and T.E. Evans, Phys. Plasmas **20**, 052505 (2013)

[64] O. Sauter, C. Angioni, and Y.R. Lin-Liu, Phys. Plasmas **6**, 2834 (1999)

[65] J. Mandrekas, "Physics Models and User's Guide for the Neutral Beam Module of the SuperCode," GTFR-102 (1992)

[66] W.M. Stacey, Phys. Plasmas **20**, 092508 (2013)

[67] W.M. Stacey and D.J. Sigmar, Phys. Fluids **28**, 2800 (1985)

[68] W.M. Stacey, A.W. Bailey, D.J. Sigmar, and K.C. Shaing, Nucl. Fusion **25**, 463 (1985)

[69] W.M. Stacey, Phys. Plasmas **21**, 092517 (2014)

[70] W.M. Stacey and C. Bae, Phys. Plasmas **22**, 062503 (2015)

[71] W.M. Stacey, Contrib. Plasma Phys. **48**, 94-98 (2008)

[72] W.M. Stacey, Fusion Plasma Physics, 2nd ed. (Wiley-VCH, Weinheim, 2012), pg. 90.

[73] F. Trintchouk, M. Yamada, H. Ji, R. M. Kulsrud and T. A. Carter, Phys. Plasmas **10**, 319 (2003)

[74] E. Viezzer, T. Pütterich, G.D. Conway, R. Dux, T. Happel, J.C. Fuchs, R.M. McDermott, F. Ryter, B. Sieglin, W. Suttrop, M. Willensdorfer, E. Wolfrum, Nucl. Fusion **53**, 053005 (2013)

[75] W.A. Houlberg, K.C. Shaing, S.P. Hirshman and M.C. Zarnstorff, Phys. Plasmas **4**, 3230 (1997)

[76] W. M. Stacey, Phys. Plasmas **15**, 012501 (2008)

[77] S. P. Hirshman and D. J. Sigmar, Nucl. Fusion **21**, 1079 (1981)

[78] B. Kim, P. H. Diamond, and R. J. Groebner, Phys. Fluids B **3**, 2050 (1991)

[79] Alexei Pankin, Douglas McCune, Robert Andre, Glenn Bateman, Arnold Kritz, Computer Physics Communications **159**, 157-184 (2004)

[80] L.L. Lao, H.S. John, R.D. Stambaugh, A.G. Kellman and W. Pfeiffer, Nucl. Fusion **25**, 1611 (1985)

[81] S. H. Müller, J. A. Boedo, K. H. Burrell, J. S. deGrassie, R. A. Moyer, D. L. Rudakov, and W. M. Solomon, Phys. Rev. Lett. **106**, 115001 (2011)

[82] T.G. Collart and W.M. Stacey, Phys. Plasmas, submitted 2016

[83] R.L. Miller, M.S. Chu, J.M. Greene, Y.R. Lin-Lin and R.E. Waltz, Phys. Plasmas **5**, 973 (1998)

[84] R.B White and M.S Chance, Phys. Fluids **13**, 2455 (1984)

[85] W.M. Stacey, Nucl. Fusion **53**, 063011 (2013)

[86] J. A. Boedo, E.A. Belli, E. Hollmann, W.M. Solomon, D.L. Rudakov, J.G. Watkins, R. Prater, J. Candy, R.J. Groebner, K.H. Burrell, J.S. deGrassie, C.J. Lasnier, A.W. Leonard, R.A. Moyer, G.D. Porter, N.H. Brooks, S. Muller, G. Tynan, and E.A. Unterberg, Phys. Plasmas **18**, 032510 (2011)

[87] C. Pan, S. Wang, and J. Ou, Nucl. Fusion **54**, 103003 (2014)

[88] R. White, Phys. Fluids B **2**, 845 (1990)

[89] A.H. Boozer, Phys. Fluids **27**, 2441 (1984)

[90] R.G. Littlejohn, Phys. Fluids **28**, 2015 (1985)

[91] K.C. Shaing, K. Ida and S.A. Sabbagh, Nucl. Fusion **55**, 125001 (2015)